INSERTION DEVICES

P. Elleaume
European Synchrotron Radiation Facility, Grenoble, France

Abstract
The characteristics of the synchrotron radiation generated by an electron beam in bending magnets, planar undulators and wiggler magnets are derived, with emphasis on the spectral flux, brilliance, and power densities. The interaction of the electron beam with the insertion device field is discussed in terms of closed orbit distortion, tune shift and non-linear effect. The technology of permanent magnet insertion devices is presented. A brief mention is made of the insertion devices used to generate circularly polarized radiation as well as undulators for free electron lasers.

1 Introduction

In the 1970s it was known that the large flux of VUV and X-ray synchrotron radiation available from the bending magnets of the first generation of storage rings dedicated to research in high-energy physics could have a large impact on many other domains of science. This radiation is indeed the most intense and powerful available at wavelengths shorter than those attainable by laser technology. The effort made to optimize the source of such radiation naturally lead to the idea of wigglers and undulators, generally called insertion devices. An insertion device can be viewed as a sequence of bending magnets of opposite polarity driving the beam in an oscillatory motion. The radiation from each bend therefore accumulates in a preferential direction producing very high spectral flux. It was very quickly recognized that the radiation from each pole interferes with the other resulting in emission spectra made of narrow peaks and peak intensity growing like the square of the number of periods. Insertion devices which are optimized to make use of the enhanced spectral flux due to the interference are now called undulators. They are built with short periods and medium fields as opposed to wigglers, which are usually optimized for large magnetic fields resulting in longer periods with negligible enhancement by interference. A review article covering the early phase of development is given in [1]. Nowadays, insertion devices are not only used to provide higher flux compared to bending magnet sources, but also to produce radiation with different polarization characteristics.

Section 2 defines the formalism used to compute synchrotron radiation properties. Sections 3, 4 and 5 apply this formalism to the cases of bending magnet radiation, undulator radiation and wiggler radiation. Section 6 deals with the perturbations induced by the magnetic field of an insertion device on the electron beam dynamics in a storage ring. Section 7 presents a short review of the engineering issues encountered with permanent magnet undulators and wigglers. Section 8 introduces two special cases of exotic undulators built either for generating an arbitrary type of polarization or for a free electron laser experiment.

This lecture is largely inspired from a multi-author book edited by the author [2]. The reader must consider this lecture as a basic introduction and should refer to [2] for a more complete and detailed presentation. One should also mention another lecture on the same topics made by R.P. Walker in a previous CERN Accelerator School [3]. The content of the present lecture has been organized to be a complement of this lecture rather than a duplication. Another detailed presentation of the characteristics of synchrotron radiation has been given by K.J. Kim [4].

2 Generalities on synchrotron radiation

Synchrotron radiation is emitted by ultra-relativistic electrons as they propagate in a magnetic field. The analytical derivation of its electric and magnetic field can be made by means of the so-called retarded potentials. The derivation is rather lengthy and technical, it can be found in text books [5]. We shall not reproduce it in this lecture but rather emphasize some important results. We assume an ultra-relativistic electron of energy γmc^2 with $\gamma >> 1$. We also assume the so-called far field approximation for which the electron emitting the radiation is far away enough from the observer so that the unit vector $\hat{n}$ directing between the electron and the observer is a constant during the electron motion. This approximation is largely justified in the large majority of cases of interest. We shall further assume for the moment that the radiation is produced by a filament and mono-energetic electron beam of current I.

Let $\frac{d\Phi}{d\Omega d\omega/\omega}(\hat{n},\omega,\hat{u})$ be the number of photons emitted per second in a direction defined by $\hat{n}$, at the frequency ω with a polarization described by the complex unit vector $\hat{u}$. In the following, we shall commonly call $\frac{d\Phi}{d\Omega d\omega/\omega}$ the angular spectral flux. It can be expressed as:

$$\frac{d\Phi}{d\Omega d\omega/\omega}(\hat{n},\omega,\hat{u}) = \alpha\frac{I}{e}\left|\vec{H}(\hat{n},\omega)\hat{u}^*\right|^2 \tag{1}$$

where $\alpha = e^2/4\pi\varepsilon_0\hbar c = 1/137$ is the fine structure constant, $\hat{u}^*$ is the complex conjugate of $\hat{u}$ and $\vec{H}(\hat{n},\omega)$ is a dimensionless field vector which is expressed as [6]:

$$\vec{H}(\hat{n},\omega) = \frac{\omega}{2\pi}\int_{-\infty}^{\infty}\hat{n}\times(\hat{n}\times\vec{\vartheta})\exp\left(i\omega(\tau-\frac{\hat{n}\vec{R}}{c})\right)d\tau \tag{2}$$

where $\vec{R}$ and $\vec{\vartheta}$ are the position and electron velocity of an electron at time τ. $\vec{H}(\hat{n},\omega)$ is a two dimensional vector always perpendicular to $\hat{n}$. The expressions of $\vec{R}$ and $\vec{\vartheta}$ are obtained by solving the Lorentz Force equation in the magnetic field $\vec{B}$:

$$\gamma m\frac{d\vec{\vartheta}}{d\tau} = e\,\vec{\vartheta}\times\vec{B}\ ,\quad \frac{d\vec{R}}{d\tau} = \vec{\vartheta} \tag{3}$$

where e and m are the charge and mass of an electron and $\gamma = 1/\sqrt{1-\vec{\vartheta}^2/c^2}$ is the relativistic factor. The vector $\vec{H}(\hat{n},\omega)$ encapsulates the information on the magnetic field producing the radiation. It is computed through (2). All spectral properties of the radiation such as the near field and far field spectral flux, and spectral brilliance, are derived from $\vec{H}(\hat{n},\omega)$ [6]. The two-dimensional complex unit vector $\hat{u}$ describing the polarization is expressed in the space orthogonal to $\hat{n}$, it is equal to $(1,0)$ for a polarization corresponding to a horizontal electric field and $(0,1)$ for a vertical electric field. A planar polarization with electric field inclined by the angle *a* with respect to the horizontal is described by the vector $(\cos(a),\sin(a))$. Finally the right and left circular polarizations are described by the vectors $(1,i)/\sqrt{2}$ and $(1,-i)/\sqrt{2}$. In the following we shall derive close expressions of $\vec{H}(\hat{n},\omega)$ for the particular magnetic field geometries of a bending magnet, undulator and wiggler. For ultrarelativistic electrons ($\gamma \gg 1$), the expression of $\vec{H}(\hat{n},\omega)$ is only appreciable for

a direction of emission $\hat{n}$ making a small angle with the electron veolicity. Then $\hat{n}$ can be approximated as:

$$\hat{n} = (\theta_x, \theta_z, 1 - \frac{\theta_x^{\,2} + \theta_z^{\,2}}{2}) \tag{4}$$

and (1) can be rewritten as

$$\frac{d\Phi}{d\Omega d\omega / \omega}(\theta_x, \theta_z, \omega, \hat{u}) = \alpha \frac{I}{e}\left|\vec{H}(\theta_x, \theta_z, \omega)\hat{u}^*\right|^2 \ . \tag{5}$$

A thick electron beam is described by a density $\rho(\theta_x, \theta_z)$ of electron travelling in the direction (θ_x, θ_z). The angular spectral flux generated by a thick electron beam is the angular convolution of $\alpha \frac{I}{e}\left|\vec{H}(\theta_x, \theta_z, \omega)\hat{u}^*\right|^2$ (angular spectral flux from a filament electron beam) with the electron distribution $\rho(\theta_x, \theta_z)$.

In synchrotron sources, another important quantity is the spectral brilliance or simply brilliance (some people use brightness instead of brilliance). It can be assimilated with the number of photons with transverse position $\vec{y} = (x, z)$ propagating in the direction $\vec{y}\,' = (\theta_x, \theta_z)$ with frequency ω and polarization $\hat{u}$. Such brilliance is observed at a longitudinal position *s* from the source. The brilliance B generated by a filament electron beam is expressed as a function of the dimensionless field vector $\vec{H}$ by means of the so-called Wigner distribution function [4,6]:

$$\begin{aligned} B(\vec{y}, \vec{y}', s, \omega, \hat{u}) = \alpha(\frac{\omega}{2\pi c})^2 \frac{I}{e} \int_{-\infty}^{\infty}\int_{-\infty}^{\infty} (\vec{H}(\vec{y}' + \vec{\xi}'/2, \omega)\hat{u}^*)(\vec{H}^*(\vec{y}' - \vec{\xi}'/2, \omega)\hat{u}) \\ \times \ \exp(-i\frac{\omega}{c}(\vec{y} - s\vec{y}')\vec{\xi}')d^2\vec{\xi}' \end{aligned} \tag{6}$$

For a thick electron beam described by a 4-dimensional density $\rho(\vec{y}, \vec{y}')$, the brilliance is a 4 dimensional convolution (in $\vec{y}$ and $\vec{y}'$) of the electron density $\rho(\vec{y}, y')$ with the brilliance generated by a filament beam expressed by (6).

3 Radiation from bending magnets

In a uniform magnetic field, the electron trajectory follows a helix. Neglecting the axial velocity parallel to the magnetic field, the motion becomes a circle with a radius of curvature $\rho = eB/mc\gamma$. Let θ be the angle between the direction of observation and the plane of the circle. The unit vector $\hat{n}$, the velocity $\vec{\vartheta}(\tau)$ and the position $\vec{R}(\tau)$ are described by:

$$\begin{aligned} \hat{n} &= (0, \theta, 1 - \frac{\theta^2}{2}) \\ \vec{\vartheta}(\tau) &= \beta(-\omega_0\tau, 0, 1 - \frac{\omega_0^{\,2}\tau^2}{2}) \\ \vec{R}(\tau) &= (-c^2\tau^2/2\rho, 0, \beta c\tau - c^3\tau^3/6\rho^2) \end{aligned} \tag{7}$$

where $\omega_0 = eB/m\gamma$ is the angular frequency of the circular motion. Replacing (7) in (2), one obtains:

$$H_x = i\frac{\omega}{\omega_c}\frac{\gamma\sqrt{3}}{2\pi}(1+\gamma^2\theta^2)K_{2/3}(\xi)$$
$$H_z = \frac{\omega}{\omega_c}\frac{\gamma\sqrt{3}}{2\pi}\gamma\theta(1+\gamma^2\theta^2)K_{1/3}(\xi) \quad (8)$$

with

$$\xi = \frac{\omega\rho}{3c}\left(\frac{1}{\gamma^2}+\theta^2\right)^{3/2} \quad , \quad \omega_c = \frac{3c\gamma^3}{2\rho} \ . \quad (9)$$

Replacing (8) in (1), one obtains in practical units [photons/s/mrad^2/0.1% bandwidth]:

$$\frac{d\Phi}{d\Omega d\omega/\omega} = 1.327\times10^{13}E^2[\mathrm{GeV}]I[\mathrm{A}]\left(\frac{\omega}{\omega_c}\right)^2\left(1+\gamma^2\theta^2\right)^2\left[K_{2/3}^2(\xi)+\frac{\gamma^2\theta^2}{1+\gamma^2\theta^2}K_{1/3}^2(\xi)\right] \ . \quad (10)$$

The critical wavelength λ_c and critical photon energy ε_c associated to ω_c are given in practical units:

$$\lambda_c[\mathrm{A}] = \frac{18.6}{B[\mathrm{T}]E^2[\mathrm{GeV}]} \ , \ \varepsilon_c[\mathrm{keV}] = 0.665B[\mathrm{T}]E^2[\mathrm{GeV}] \ . \quad (11)$$

The vertical angular divergence of both horizontal and vertical field components depends on the photon energy (Fig. 1). At a photon energy close to the critical energy, the horizontal component H_x^2 is reasonably well approximated by a Gaussian distribution with a standard deviation $\sigma_R^{'}$ given by [7]:

$$\sigma_R^{'} \approx \frac{0.565}{\gamma}\left(\frac{\omega}{\omega_c}\right)^{-0.425} \ . \quad (12)$$

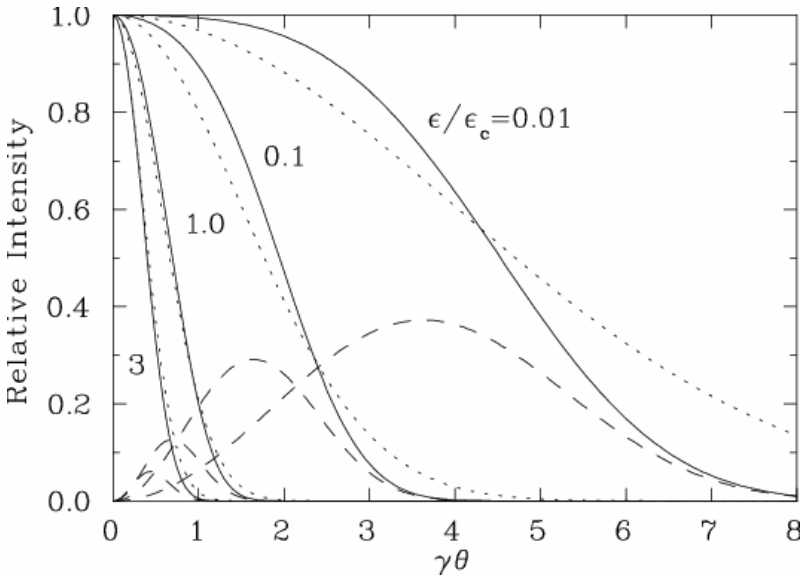

Fig. 1: Angular distribution of H_x^2, (solid line), and H_z^2, (dashed lines), the horizontal and vertical polarized radiation as a function of the normalized vertical angle for various photon energies. The dotted line is the expression given by Eq. (12). For each photon energy an identical normalization has been applied to both H_x^2 and H_z^2 in such a way that $H_x^2(\theta=1)=1$. Illustration from Ref. [7].

On axis $\theta = 0$, only the horizontal polarization exists and (10) is rewritten as:

$$\left.\frac{d\Phi}{d\Omega d\omega/\omega}\right|_{\theta=0} = 1.327\times10^{13} E^2[\mathrm{GeV}] I[\mathrm{A}] H_2\left(\frac{\omega}{\omega_c}\right) \tag{13}$$

with $H_2(y) = y^2 K_{2/3}^2\left(\frac{y}{2}\right)$. Figure 2 shows the function $H_2(y)$, which peaks at $\frac{\omega}{\omega_c} = \frac{\varepsilon}{\varepsilon_c} = 0.83$.

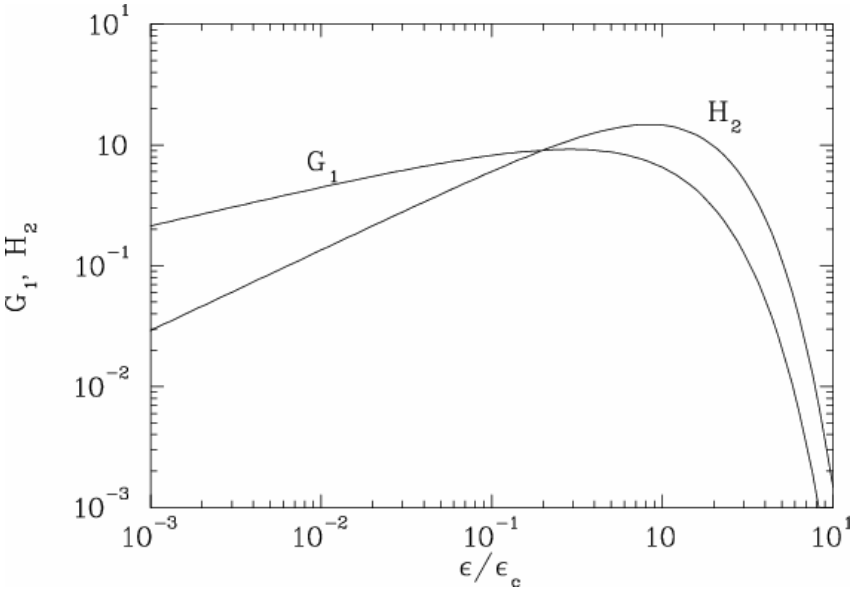

Fig. 2: The functions $H_2(y)$ and $G_1(y)$. Illustration from Ref. [7].

It results from (8) that H_z is real while H_x is imaginary; as a result the polarization is elliptical out of the orbit plane. At large angles both components have similar amplitude and the polarization is fully circularly polarized right (left) handedly above (below) the orbit plane respectively.

Integrating the flux $\frac{d\Phi}{d\Omega d\omega/\omega}$ over the vertical angle θ, one obtains the photon flux per relative bandwidth per unit horizontal angle:

$$\frac{d\Phi}{d\Omega d\omega/\omega} = 2.457\times10^{13} E[\mathrm{GeV}] I[A] G_1\left(\frac{\omega}{\omega_c}\right) \tag{14}$$

where the function $G_1(y) = y\int_y^\infty K_{5/3}(y')dy'$ is presented in Fig. 2. Integrating (10) over all frequencies, one derives the power density in practical units:

$$\frac{dP}{d\Omega}[\mathrm{W/mrad^2}] = 5.42 E^4[\mathrm{GeV}] B[\mathrm{T}] I[\mathrm{A}] \frac{1}{\left(1+\gamma^2\theta^2\right)^{5/2}}\left[1+\frac{5\gamma^2\theta^2}{7\left(1+\gamma^2\theta^2\right)}\right] \tag{15}$$

The first (second) term in the brackets corresponds to horizontally (vertically) polarized radiation. This distribution is well approximated by a Gaussian with standard angular deviation σ [7]:

$$\sigma = \frac{0.608}{\gamma} \ . \tag{16}$$

Integrating (15) over the vertical angle, one obtains the Power per unit horizontal angle:

$$\frac{dP}{d\theta_x}[\mathrm{W/mrad}] = 4.221 E^3[\mathrm{GeV}] B[\mathrm{T}] I[\mathrm{A}] \ . \tag{17}$$

One can show that half of the angular power given by (17) corresponds to photon energies below and above the critical energy ε_c. The total power generated in all bending magnets is obtained by multiplying (17) by 2000π. It is clear from the previous results that the power and power densities are a steep function of the electron energy. As an illustration, Table 1 presents the power and power densities from three very different electron storage rings with energies ranging from 0.8 to 6 GeV.

Table 1: Main parameters of synchrotron radiation facilities of three typical energies. The power is the total power generated in all bending magnets along the circumference. Both the power and power density are strongly dependent on the electron energy.

Ring	**Energy [GeV]**	**Field [T]**	ε_c **[keV]**	**Current [A]**	**Power [kW]**	$dP/d\Omega$ **[W/mrad^2]**
SuperACO	0.8	1.57	0.67	0.4	8.5	1.4
ELETTRA	2	1.2	3.2	0.3	76	31.2
ESRF	6	0.85	20.3	0.2	974	1194

4 Radiation from planar undulators

In the following we shall use the following notation:

$$\vec{A} = (A_x, A_z, A_s) \tag{18}$$

where A_x, A_z and A_s are respectively the horizontal, vertical and longitudinal components of the field vector $\vec{A}$. An undulator field will be described as a vertical field with sinusoidal dependence on the longitudinal coordinate *s*:

$$\vec{B} = \left(0, -\hat{B}\sin(2\pi\frac{s}{\lambda_0}), 0\right) \ . \tag{19}$$

Let us consider an electron propagating along the *s* axis and injected inside the undulator with no initial velocity, then integrating the Lorentz force equation (3) gives the velocity $\vec{\vartheta}$ and position $\vec{R}$:

$$\begin{aligned} \vec{\vartheta} &= \left(\frac{K}{\gamma}\cos(2\pi\frac{s}{\lambda_0}), 0, 1\right) + o(\frac{1}{\gamma}) \\ \vec{R} &= \left(\frac{K\lambda_0}{2\pi\gamma}\sin(2\pi\frac{s}{\lambda_0}), 0, s\right) + o(\frac{1}{\gamma}) \end{aligned} \tag{20}$$

where $s \approx c\tau$ is the longitudinal coordinate of the electron. $o(\frac{1}{\gamma})$ is a quantity of an order smaller than $\frac{1}{\gamma}$. *K* is the deflection parameter expressed as:

$$K = \frac{e\hat{B}\lambda_0}{2\pi mc} = 0.0934\hat{B}[\mathrm{T}]\lambda_0[\mathrm{mm}] \ . \tag{21}$$

The periodicity of the trajectory allows the rewriting of the field vector (2) as:

$$\vec{H}(\theta_x,\theta_z,\omega) = \vec{h}(\theta_x,\theta_z,\omega)\left(\sum_{q=-(N-1)/2}^{(N-1)/2} \exp(2i\pi q\frac{\omega}{\omega_1})\right) = N\vec{h}(\theta_x,\theta_z,\omega)\frac{\sin(\pi N\frac{\omega}{\omega_1})}{N\sin(\pi\frac{\omega}{\omega_1})} \tag{22}$$

where $\vec{h}(\theta_x,\theta_z,\omega)$ is formally identical to the function $\vec{H}(\theta_x,\theta_z,\omega)$ but the time integration in (2) is limited to the motion over a single undulator period and N is the number of undulator periods. The frequency ω_1 and its associated wavelength λ_1 are expressed as:

$$\omega_1 = \frac{4\pi c\gamma^2}{\lambda_0\left(1+\frac{K^2}{2}+\gamma^2\theta_x^2+\gamma^2\theta_z^2\right)} \ , \qquad \lambda_1 = \frac{2\pi c}{\omega_1} = \frac{\lambda_0}{2\gamma^2}\left(1+\frac{K^2}{2}+\gamma^2\theta_x^2+\gamma^2\theta_z^2\right) \ . \tag{23}$$

The associated photon energy E_1 can be expressed in dimensionless units:

$$E_1[\mathrm{keV}] = \frac{h\omega_1}{2\pi} = 0.95\frac{E^2[\mathrm{GeV}]}{\lambda_0[\mathrm{cm}](1+\frac{K^2}{2})} \ . \tag{24}$$

Figure 3 presents the variation of $\frac{\sin(\pi N\,\omega/\omega_1)}{N\sin(\pi\,\omega/\omega_1)}$ as a function ω/ω_1. Since the spectral flux scales like the modulus square of $\vec{H}(\theta_x,\theta_z,\omega)$, it clearly appears that the radiation spectrum is concentrated on the frequency ω_1 and its harmonics.

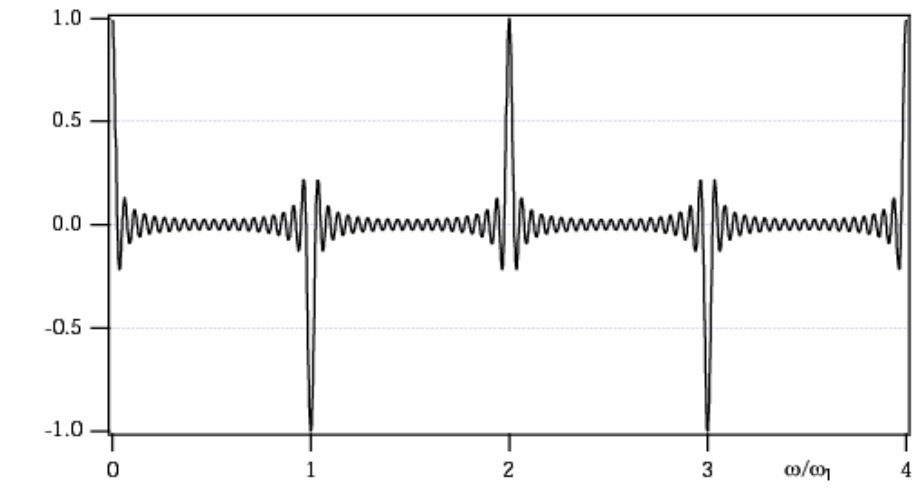

Fig. 3: Function $\frac{\sin(\pi N\,\omega/\omega_1)}{N\sin(\pi\,\omega/\omega_1)}$ as a function of ω/ω_1 in the particular case of $N = 40$ periods

In the limit of a large number of periods N, one can approximate:

$$\frac{\sin(\pi N\,\omega/\omega_1)}{N\sin(\pi\,\omega/\omega_1)} \approx \sum_{n=1,2...}^{\infty} (-1)^{n(N-1)}\,\frac{\sin(\pi N\,\omega/\omega_1 - n)}{\pi N\sin(\omega/\omega_1 - n)} \tag{25}$$

and one approximates the field vector $\vec{H}(\theta_x,\theta_z,\omega)$ as:

$$\vec{H}(\theta_x,\theta_z,\omega) \approx N\sum_{n=1}^{\infty}(-1)^{n(N-1)}\vec{h}_n(\theta_x,\theta_z)\frac{\sin(\pi N\,\omega/\omega_1 - n)}{\pi N\sin(\omega/\omega_1 - n)} \tag{26}$$

where $\vec{h}_n(\theta_x,\theta_z) = \vec{h}(\theta_x,\theta_z,n\omega_1)$. Replacing (20) into (2) and performing an integration over a single period, one derives the following expression for $\vec{h}_n(\theta_x,\theta_z)$:

$$\vec{h}_n(\theta_x,\theta_z) = \frac{n}{\lambda_1}\int_0^{\lambda_0}\begin{bmatrix}\frac{K}{\gamma}\cos(2\pi\,s/\lambda_0) - \theta_x \\ -\theta_z\end{bmatrix}\times$$

$$\times\exp\left(2i\pi n\left(\frac{s}{\lambda_0} + \frac{-2\gamma\theta_x K\sin(2\pi\,s/\lambda_0) + (K^2/4)\sin(4\pi\,s/\lambda_0))}{2\pi(1+K^2/2+\gamma^2\theta_x^2+\gamma^2\theta_z^2)}\right)\right) \tag{27}$$

Replacing (26) into (1), one derives the angular spectral flux $\frac{d\Phi}{d\Omega d\omega/\omega}(\hat{n},\omega,\hat{u})$:

$$\frac{d\Phi}{d\Omega d\omega/\omega}(\theta_x,\theta_z,\omega,\hat{u}) \approx \alpha\frac{I}{e}N^2\sum_{n=1}^{\infty}\left|\vec{h}_n(\theta_x,\theta_z)\hat{u}^*\right|^2\left|\frac{\sin(\pi N\,\omega/\omega_1 - n)}{\pi N\sin(\omega/\omega_1 - n)}\right|^2 . \tag{28}$$

Figure 4 presents the variation of $\frac{d\Phi}{d\Omega d\omega/\omega}(\hat{n},\omega,\hat{u})$ versus ω/ω_1 computed for a $N = 20$ period undulator. The spectrum is made up of a series of harmonics. The angular spectral flux $\frac{d\Phi_n}{d\Omega d\omega/\omega}$ at the top of the n^{th} peak is given by:

$$\frac{d\Phi_n}{d\Omega d\omega/\omega} \approx \alpha\frac{I}{e}N^2\left|\vec{h}_n(\theta_x,\theta_z)\hat{u}^*\right|^2 . \tag{29}$$

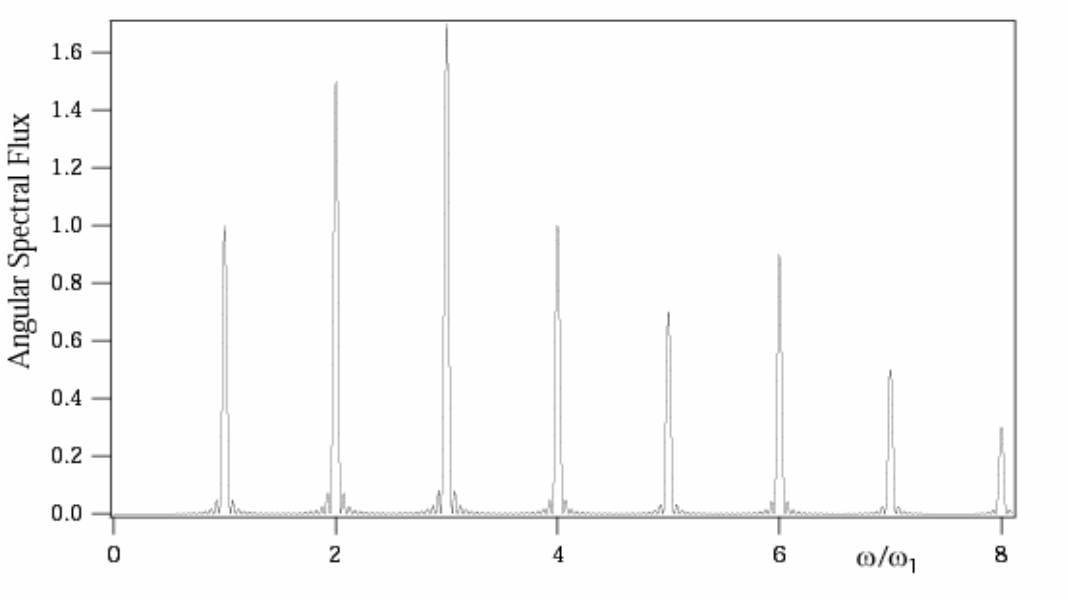

Fig. 4: Angular spectral flux $\frac{d\Phi}{d\Omega d\omega/\omega}$ as a function of ω/ω_1 for N = 20 a periods undulator

The height of each harmonic is therefore proportional to $\left|\vec{h}_n\hat{u}^*\right|^2$. The harmonics have a relative narrow spectral width $\Delta\omega/\omega_1 \sim 1/nN$. The shape of the harmonic n is determined by the function $\left|\frac{\sin(\pi N\,\omega/\omega_1 - n)}{\pi N \sin(\omega/\omega_1 - n)}\right|^2$. The fact that the spectrum is made up of a series of harmonics is a consequence of the periodicity of the undulator field. The details of the undulator field over one period enters in the expression of the resonant frequency ω_1 and in the relative emission on each harmonic by means of the quantity $\left|\vec{h}_n\hat{u}^*\right|^2$. Figure 5 presents a plot of $\left|\vec{h}_n\hat{u}^*\right|^2$ as a function of the normalized horizontal and vertical angle of observation $\gamma\theta_x$ and $\gamma\theta_z$. The computation is made on the first three harmonics n = 1, 2 and 3 and for a K = 2 undulator. The plain contour lines correspond to the horizontal polarization $\left|\vec{h}_n\hat{u}_x^*\right|^2$ while the dash contour corresponds to the vertical polarization $\left|\vec{h}_n\hat{u}_z^*\right|^2$. The intensity in the vertical polarization is typically 5–10 times weaker than in the horizontal polarization. Harmonics 1 and 3 (and all odd harmonics) have a peak of emission on axis [$(\theta_x,\theta_z) = (0,0)$]. In this direction, the radiation is fully linearly polarized with a horizontal electric field. Harmonics 2 (and all even harmonics) have a minimum of emission on axis. Using the expression (27) of $\vec{h}_n(\theta_x,\theta_z)$, one can also show that the higher the harmonic number, the higher the number of lobes in $\left|\vec{h}_n\hat{u}_x^*\right|^2$ and $\left|\vec{h}_n\hat{u}_z^*\right|^2$.

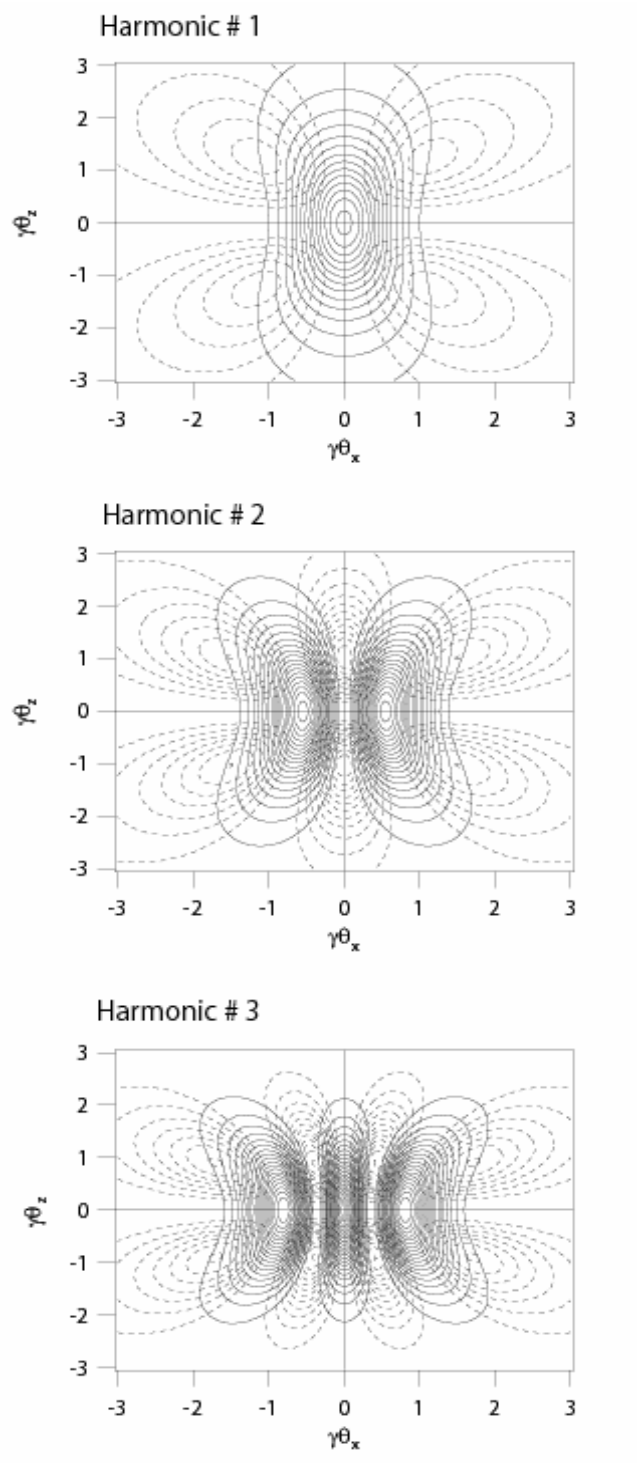

Fig. 5: Contour plot of $\left|\vec{h}_n \hat{u}_x^{\,*}\right|^2$ (plain) and $\left|\vec{h}_n \hat{u}_z^{\,*}\right|^2$ (dashed) as a function of $\gamma\theta_x$ and $\gamma\theta_z$ for $K = 2$.

The expression of $\vec{h}_n(0,0)$ on axis of the undulator is of great importance since it corresponds to the maximum in the angular spectral flux. It is derived from (27) and, for an odd harmonic *n*, it can be expressed as:

$$\vec{h}_n(0,0) = \gamma\hat{u}_x \frac{nK}{1+K^2/2}\left[J_{(n+1)/2}\left(\frac{nK^2}{4+2K^2}\right) - J_{(n-1)/2}\left(\frac{nK^2}{4+2K^2}\right)\right] \tag{30}$$

while $\vec{h}_n(0,0) = 0$ for an even harmonic *n*. Replacing (30) in (29), one obtains the angular spectral flux on axis on harmonics *n*

$$\begin{aligned} \frac{d\Phi_n}{d\Omega d\omega/\omega} &\approx \alpha\frac{I}{e}N^2\gamma^2 F_n(K) \ , \quad \text{with} = 1,3,5... \\ \frac{d\Phi_n}{d\Omega d\omega/\omega} &\approx 0 \ , \quad \text{with} = 2,4,6... \end{aligned} \tag{31}$$

or in dimensionless units for an odd harmonic:

$$\frac{d\Phi_n}{d\Omega d\omega/\omega}[\text{Photons/s/0.1\%/mrad}^2] \approx 1.744\times10^{14} N^2 E^2[\text{GeV}] I[\text{A}] F_n(K) \tag{32}$$

The dimensionless quantity $F_n(K)$ is given by

$$F_n(K) = \frac{n^2K^2}{\left(1+K^2/2\right)^2}\left[J_{(n+1)/2}\left(\frac{nK^2}{4+2K^2}\right) - J_{(n-1)/2}\left(\frac{nK^2}{4+2K^2}\right)\right]^2 \tag{33}$$

where $J_n(x)$ is the usual Bessel function of order *n*. Figure 6 presents a plot of $F_n(K)$ as a function of *K* for *n* = 1,3,5 and 7.

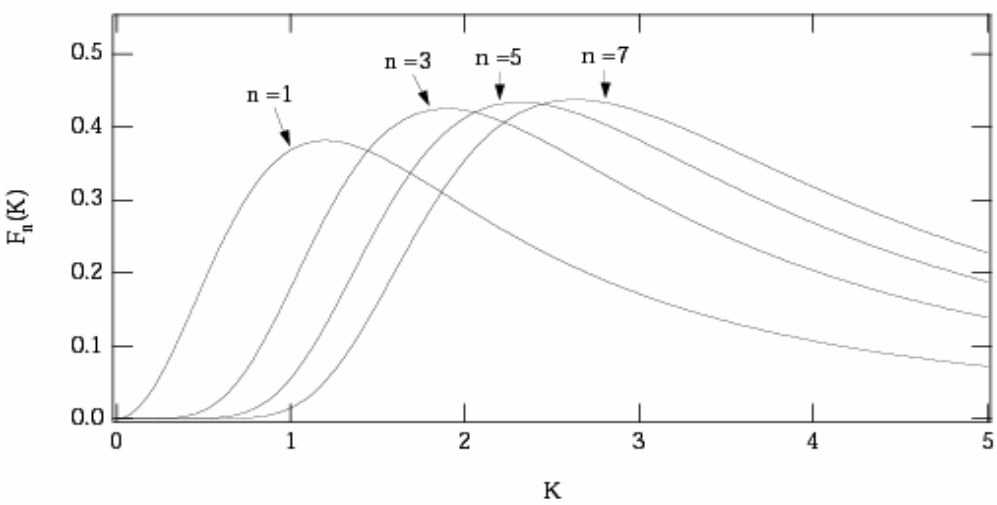

Fig. 6: Plot of $F_n(K)$ as a function of *K* for *n* = 1,3,5 and 7

Assuming a small angle ($\gamma\theta_x, \gamma\theta_z << 1$), and a large number of periods ($N >> 1$), and a not too high harmonic number *n*, the dependence of $\frac{\sin(\pi N\,\omega/\omega_1 - n)}{\pi N \sin(\omega/\omega_1 - n)}$ versus θ_x, θ_z ω is much more rapid than that of $\vec{h}_n(\theta_x, \theta_z)$ and (26) can be rewritten neglecting the variations of $\vec{h}_n(\theta_x, \theta_z)$:

$$\vec{H}(\theta_x, \theta_z, \omega) \approx N \sum_{n=1}^{\infty} (-1)^{n(N-1)} \vec{h}_n(\theta_x, \theta_z) \frac{\sin(\Gamma)}{\Gamma} \tag{34}$$

with

$$\Gamma = \pi n \frac{\theta_x^2 + \theta_z^2}{2} \frac{L}{\lambda_1(0)} + \pi N \left(\frac{\lambda_1(0)}{\lambda} - n\right) \tag{35}$$

where the on-axis wavelength $\lambda_1(0)$ is:

$$\lambda_1(0) = \frac{\lambda_0}{2\gamma^2}\left(1 + \frac{K^2}{2}\right) \quad . \tag{36}$$

The angular width of an harmonic peak around the axis can be derived from (35)and (36) to be

$$\Delta\theta \sim \frac{1}{\gamma}\sqrt{\frac{1 + K^2/2}{nN}} \quad . \tag{37}$$

In other words, when observed at the wavelength $\lambda_1(0)$ given by (36), the peaks observed on axis of the undulator are not only narrow in frequency but they are also generated over a narrow cone of emission. The angular width of the peaks of undulator emission is typically $\sqrt{\frac{1 + K^2/2}{nN}}$ narrower than the angular divergence of bending magnet radiation. Let us define the angle integrated spectral flux $\frac{d\Phi}{d\omega/\omega}$ as:

$$\frac{d\Phi}{d\omega/\omega}(\omega, \hat{u}) = \int_{-\infty}^{+\infty} \int_{-\infty}^{+\infty} \frac{d\Phi}{d\Omega d\omega/\omega}(\theta_x, \theta_z, \omega, \hat{u}) d\theta_x d\theta_z \quad . \tag{38}$$

In general, its detailed expression is rather involved. If one restricts the frequency ω to the most interesting case of the on-axis frequency $\omega_n = n\omega_1(0,0)$, assuming $N >> 1$, one can make use of (34) and (35) to obtain:

$$\frac{d\Phi_n}{d\omega/\omega} = \frac{d\Phi}{d\omega/\omega}(\omega_n, \hat{u}) \approx \pi\alpha N \frac{I}{e} Q_n(K) \left| u_x \hat{u}^* \right|^2 \tag{39}$$

It is linearly polarized in the horizontal plane. It can be written in dimensionless units:

$$\frac{d\Phi_n}{d\omega/\omega}[\text{Photons/s/0.1\%}] \approx 1.431 \times 10^{14}\, NI[\text{A}] Q_n(K) \tag{40}$$

where the dimensionless quantity $Q_n(K)$ is expressed as

$$Q_n(K) = (1+K^2/2)\frac{F_n(K)}{n} = \frac{nK^2}{1+K^2/2}\left[J_{(n+1)/2}\left(\frac{nK^2}{4+2K^2}\right) - J_{(n-1)/2}\left(\frac{nK^2}{4+2K^2}\right)\right]^2 . \qquad (41)$$

Figure 7 presents a plot of $Q_n(K)$ versus *K* for several odd harmonic numbers *n.*

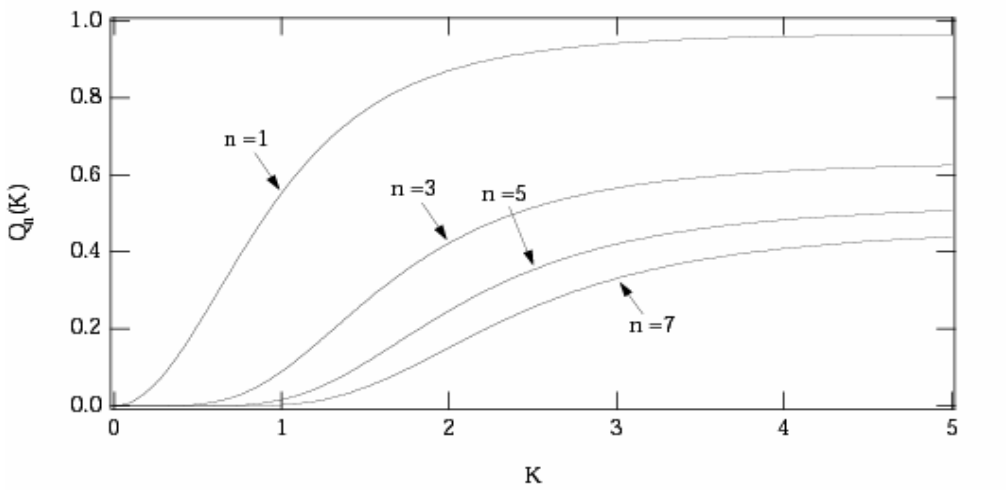

Fig. 7: Plot of $Q_n(K)$ vs. *K*

So far we have assumed a filament mono-energetic electron beam. In view of the very narrow peaks of the undulator emission (in both energy and angle), one can expect that the shape and width of the peaks can be strongly affected by the electron energy spread and the angular divergence of the electron beam. In addition, in a real experiment, an observer integrates the spectral flux over a finite aperture and the size of the aperture defines a spread in the direction in which the radiation is collected. For similar reasons, the electron beam sizes contribute to the broadening of the radiation. The precise computation of the undulator peaks broadened by the electron energy spread, angular divergence and beam sizes is best carried out using numerical tools. Figure 8 presents such a spectrum computed for an ESRF undulator observed through a slit:

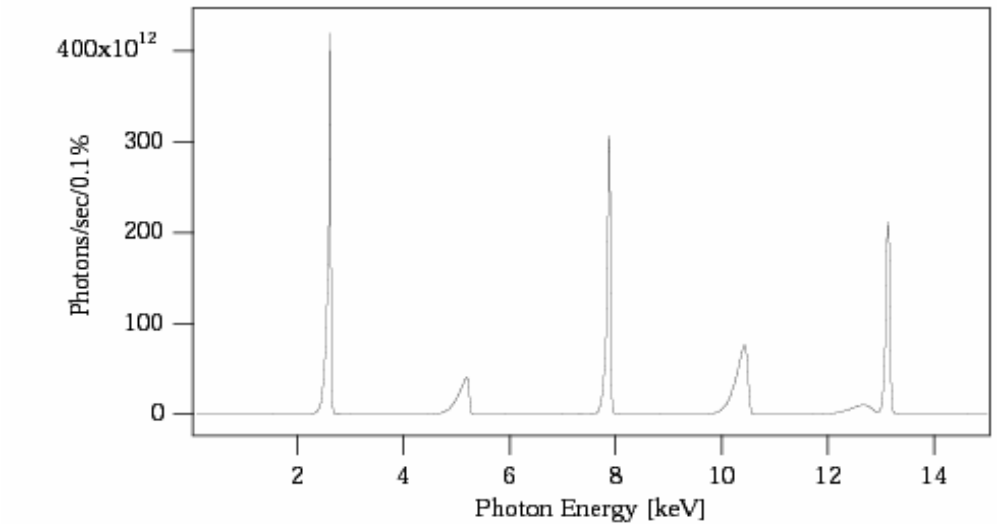

Fig. 8: Spectrum through a slit produced by an undulator of the ESRF

It is clear from Fig. 8 that the broadening affects each peak in a non-symmetrical fashion. The tails are longer on the low energy side. This can be traced to the dependence of ω_1 on $\left(1+\frac{K^2}{2}+\gamma^2\theta_x^2+\gamma^2\theta_z^2\right)^{-1}$ which shifts ω_1 toward lower values whenever θ_x and θ_z deviates from 0. The shape of the profile of the high-energy side of the peak is determined by the electron energy spread and the undulator field errors. Since the energy of the peak of the undulator emission scales proportionally to the square of the electron energy, it appears that even a filament electron beam, but with a non-zero energy spread, introduces a broadening of the peaks. The undulator magnetic field contains a number of errors which also broaden the spectrum. Since high harmonic numbers are naturally narrow ($\sim 1/nN$), the higher the harmonics the more sensitive they are to the energy spread, electron beam emittance and field errors.

We have seen that one of the main features of the undulator emission is its small divergence and spectral width. A typical figure of merit of undulator radiation is the spectral brightness or spectral brilliance. The brilliance was introduced in Section 2, it is the number of photons emitted per unit spectral bandwidth, per unit solid angle and per unit source size. Of most importance is the brilliance on axis on odd harmonics which can be approximated as:

$$B_n \approx \frac{\dfrac{d\Phi_n}{d\omega/\omega}}{(2\pi)^2\,\Sigma_x\Sigma_{x'}\Sigma_z\Sigma_{z'}} \tag{42}$$

where $\dfrac{d\Phi_n}{d\omega/\omega}$ is the angle integrated spectral flux expressed by (39) and Σ_x and $\Sigma_{x'}$ (Σ_z and $\Sigma_{z'}$) are the horizontal (vertical) r.m.s. photon beam size and divergence. Their expression is the convolution of a contribution from the electron beam as well as a so-called diffractive contribution which comes from the wave nature of the radiation. Their expressions are:

$$\begin{aligned} \Sigma_{x'}^2 &\approx \sigma_{x'}^2 + \lambda/2L \quad , \quad \Sigma_{z'}^2 \approx \sigma_{z'}^2 + \lambda/2L \\ \Sigma_x^2 &\approx \sigma_x^2 + \lambda L/8\pi^2 \quad , \quad \Sigma_z^2 \approx \sigma_z^2 + \lambda L/8\pi^2 \end{aligned} \tag{43}$$

in which σ_x and $\sigma_{x'}$ (σ_z and $\sigma_{z'}$) are the horizontal (vertical) electron beam size and divergence. By changing the peak magnetic field of an undulator, one modifies the *K* values and therefore the energy of the harmonics. A classical way to summarize the undulator performance on a particular machine is to plot the on-axis brilliance B_n as a function of the photon energy for each harmonic. Figure 9 presents such a plot. According to the photon energy of interest, a user would select one or the other harmonics. For some beamlines it is important to cover a wide photon energy range continuously. This can be done if one uses an undulator with maximum *K* value larger than 2.2.

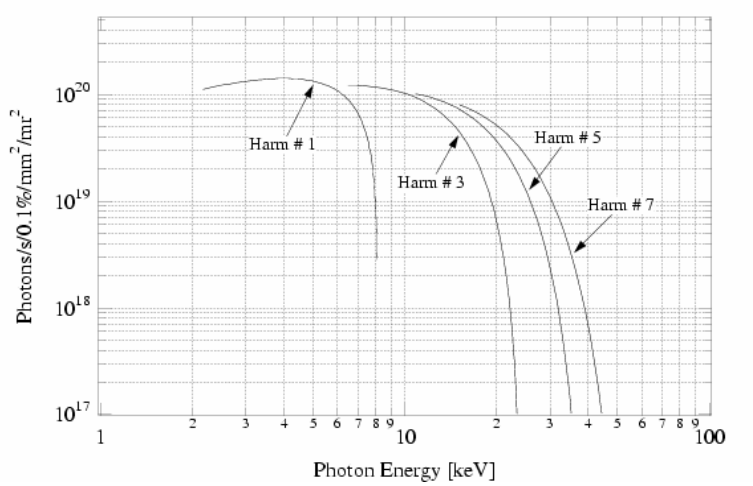

Fig. 9: Brilliance produced by a 5 m long undulator having a period of 42 mm and a maximum *K* of 2.4 installed on a high-beta straight section of the ESRF ring

We have given expressions for the angular flux, angle integrated flux and brilliance of the undulator emission. For reasons of completeness, one must mention the expression of the power density of the radiation. Such quantities are also of prime importance in the design of the absorbers and beamlines optical components. We shall simply give its expression. For a filament electron beam, the power density $\frac{dP}{d\Omega}$ emitted in a direction (θ_x, θ_z) is given by [8]:

$$\frac{dP}{d\Omega}(\theta_x,\theta_z) = \frac{e^2}{4\pi\varepsilon_0}\frac{2\gamma^4}{\pi}\frac{I}{e}NK^2\frac{4\pi^2}{\lambda_0^2}\int_{-\lambda_0/2}^{\lambda_0/2}\left(\frac{1}{d^3} - 4\frac{(\gamma\theta_x - K\cos(2\pi\, s/\lambda_0))^2}{d^5}\right)\sin^2(2\pi\, s/\lambda_0)ds \qquad (44)$$

where *d* is expressed as:

$$d = 1 + \left(\gamma\theta_x - K\cos(2\pi\, s/\lambda_0)\right)^2 + \left(\gamma\theta_z\right)^2 . \qquad (45)$$

Integrating $\frac{dP}{d\Omega}(\theta_x,\theta_z)$ over all angles (θ_x,θ_z), one obtains the total power *P*:

$$P = 2\pi ecZ_0 I\gamma^2\frac{NK^2}{6\lambda_0} \qquad (46)$$

with $Z_0 = 377$ ohm. In practical units:

$$P[\mathrm{kW}] = 0.633E^2[\mathrm{GeV}]\hat{B}^2[\mathrm{T}]L[\mathrm{m}]I[\mathrm{A}] \qquad (47)$$

the on-axis power density can be expressed as

$$\frac{dP}{d\Omega}(0,0) = P\frac{21\gamma^2}{16\pi K}G(K) \qquad (48)$$

or in practical units

$$\frac{dP}{d\Omega}(0,0)[\mathrm{W/mrad^2}] = 10.84\hat{B}[\mathrm{T}]E^4[\mathrm{GeV}]I[\mathrm{A}]NG(K) \qquad (49)$$

with $G(K)$ defined as:

$$G(K) = K \frac{K^6 + 24/7\, K^4 + 4K^2 + 16/7}{(1+K^2)^{7/2}} \quad . \tag{50}$$

In this section we have described in some detail the various steps of the analytical derivation of the spectral characteristics of undulator radiation. A number of people have been addressing the question for many years both analytically and numerically. As a result there exists several computer codes available for accurately computing undulator radiation. Here are some of them: B2E [9], SPECTRA [10], SRW [11], URGENT [12], XOP [13].

5 Radiation from wigglers

In the previous section we described the characteristics of the radiation generated by an electron beam travelling in the periodic magnetic field of an undulator. For large field and/or large period undulators, K is large and the energy of the fundamental drops to a low value. The radiation spectrum from such a device presents a large number of harmonics. The number n of harmonics can be estimated by comparing the equation for the wavelength of the harmonics (24) with that of the critical wavelength λ_c associated with the peak magnetic field (11). This gives rise to the following expression for the harmonic number n corresponding to a wavelength λ:

$$n = \frac{3}{4} K \frac{1+K^2/2}{\lambda/\lambda_c} \quad . \tag{51}$$

The radiation generated by a $K = 5$ (10) undulator observed at the wavelength λ_c corresponds to an harmonic number 50 (383). As discussed in the previous section, the line width of each harmonic is degraded by the electron energy spread, the emittance and the volume of phase space over which the radiation is integrated. At a sufficiently high harmonic number, the spectrum of an harmonic n overlaps with that of the harmonic $n-1$ and $n+1$. This is illustrated in Fig. 10 for a K = 5 device.

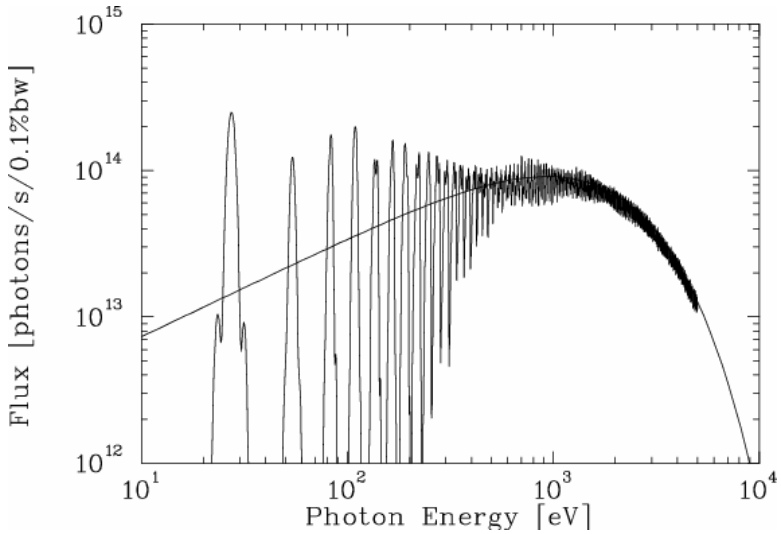

Fig. 10: Spectral flux of a K = 5 device calculated using the undulator radiation method and with the wiggler method (smooth curve). The electron energy is 2 GeV, the number of periods is $N = 10$ and the period 100 mm. The radiation is integrated over a total acceptance angle of +/- 0.2 mrad. Illustration from Ref. [7].

The low-energy part of the spectrum presents an undulator-type spectrum with well-defined harmonics while at high energy the harmonic peaks overlap each other to produce a continuous spectrum. The higher the energy, the smoother the spectrum. Superimposed to the exact computation, Fig. 10 presents an approximation called the wiggler approximation. The wiggler approximation consists in approximating the spectrum by that of a bending magnet, the field of which is equal to the peak field $\hat{B}$ multiplied by $2N$, where N is the number of periods. In other words, in the wiggler model the device is approximated as a series of $2N$ source points. There are two source points per period. Each source point takes place at a longitudinal position *s* such that the electron velocity is pointing towards the observer. We have seen [see (19) and (20)] that if the vertical field is a sine function of the longitudinal coordinate *s*, the horizontal velocity is a cosine function. As a result the electron trajectory can be represented in a field versus velocity diagram as a circle. This is illustrated in Fig. 11.

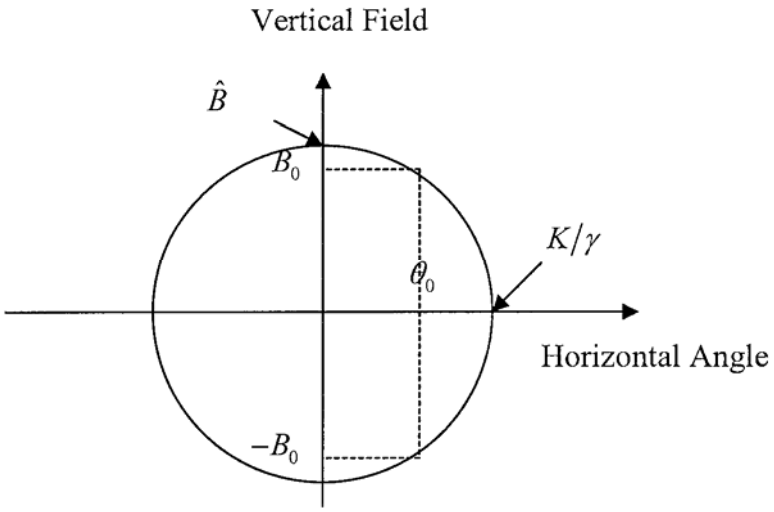

Fig. 11: Diagram of vertical field versus electron horizontal angle. In this representation, an electron makes one circle every period. The electron velocity points towards an observer in a direction θ_0 twice per period. This takes place at longitudinal coordinates such that the magnetic field is equal to B_0 and $-B_0$ as shown.

The maximum angle is equal to K/γ and is reached for a zero magnetic field. On the other hand, the maximum field is $\hat{B}$ and is reached when the angle is zero. If one observes the radiation at some non-zero angle θ_0, one sees an electron twice per period at places where the magnetic fields are B_0 and $-B_0$ (see Fig. 11). Using (19) and (20), the field of the source point B_0 can be expressed as a function of the horizontal angle θ_0:

$$\frac{B_0}{\hat{B}} = \sqrt{1-\left(\frac{\gamma\theta_0}{K}\right)^2} \quad . \tag{52}$$

To conclude, a wiggler spectrum is computed as the one produced by 2*N* bending magnets but with a critical energy that varies with the angle of observation in the horizontal plane according to (52). The polarization of the wiggler radiation can also be deduced from the polarization of bending magnet radiation. There is nevertheless one important particularity. Since there are two source points per period with equal and opposite fields, the left handed and right handed circular polarization generated above and below the orbit planes cancel each other to the point that no circularly polarized radiation is

generated from a wiggler. Indeed the polarization of the radiation is evolving from nearly 100% linearly polarized when observed in the orbit plane to fully depolarized when observed far above or below the orbit plane. In an arbitrary direction the radiation is partially linearly polarized and partially depolarized.

The detailed computation of the brilliance generated by a wiggler is out of the scope of this lecture. We summarize the main results here, namely the on-axis brilliance of wiggler radiation can be approximated [7] as:

$$B \approx \left.\frac{d\Phi}{d\Omega d\omega/\omega}\right|_{\theta_z=0} \quad \frac{N\sigma_R^{'}}{2\pi\sqrt{\sigma_z^{'2}+\sigma_R^{'2}}\sqrt{\sigma_x^2+a^2+L^2\sigma_x^{'2}/12}\sqrt{\sigma_z^2+L^2\sigma_z^{'2}/12}} \tag{53}$$

where:

$\left.\frac{d\Phi}{d\Omega d\omega/\omega}\right|_{\theta_z=0}$ is the angular spectral flux produced in the orbit plane generated by a filament electron beam in a bending magnet with field $\hat{B}$. It is given by Eq. (13).

$\sigma_R^{'}$ is the r.m.s. standard deviation of the bending magnet radiation approximated by (12);

$L = N\lambda_0$ is the wiggler length;

$\sigma_x, \sigma_x^{'}, (\sigma_z, \sigma_z^{'})$ are the horizontal (vertical) r.m.s. electron beam size and divergence;

$a = \frac{\lambda_0}{2\pi}\frac{K}{\gamma}$ is the amplitude of the sinusoidal motion of the electron in the horizontal plane.

Note that this expression only applies on axis and assumes $L \le 4\beta_z, L \le 2\beta_x, a \le \sigma_x, \sigma_z^{'} \le \sigma_R^{'}/2$. If one observes the radiation off axis in the horizontal plane, the 2*N* source points appear laterally displaced. More precisely, if one tries to refocus some bending magnet radiation generated off axis in a direction θ_x, one observes a spread of all 2*N* source points horizontally over a distance equal to $L\theta_x$.

6 Effects on the beam

6.1 Perturbation to the lattice, synchrotron radiation integrals

There is a particular difficulty with insertion devices in a storage ring. Contrary to the other lattice magnets (dipoles, quadrupoles, sextupoles), it is of prime importance for the users to vary the field in order to tune the spectral characteristics of the radiation to their particular need. It is therefore necessary for a synchrotron light source to operate with a large number of insertion devices the fields of which are changed randomly under the full control of the users. This change in field generates perturbations to the stored beam which may affect the other users. In this section we shall discuss these perturbations.

Many global characteristics of the electron beam dynamics can be deduced from the so-called synchrotron radiation integrals [14] :

$$I_2 = \oint_C \frac{1}{\rho^2} ds \quad I_3 = \oint_C \frac{1}{|\rho|^3} ds$$
$$I_4 = \oint_C \frac{(1-2n)\eta}{\rho^3} ds \quad I_5 = \oint_C \frac{\gamma_x \eta^2 + 2\alpha_x \eta\eta' + \beta_x \eta'^2}{|\rho|^3} ds \tag{54}$$

where β_x is the horizontal betatron function, $\alpha_x = -\frac{1}{2}\frac{d\beta_x}{ds}$ and $\gamma_x = \frac{1+\alpha_x^2}{\beta_x}$. η is the dispersion function and $\eta' = \frac{d\eta}{ds}$. The integrals are computed over the ring circumference. ρ is the radius of curvature which is deduced from the magnetic field *B* by means of the Lorentz force equation (3):

$$\frac{1}{\rho} = \frac{eB}{\gamma mc} \ . \tag{55}$$

A very important physical quantity derived from the I_2 integral is the energy loss per turn U_0:

$$U_0 = \frac{2}{3} r_e \gamma^4 mc^2 I_2 \ . \tag{56}$$

The damping partition numbers J_i which enter in the damping times and in the electron beam sizes, are given by:

$$J_x = 1 - \frac{I_4}{I_2} \quad J_z = 1 \quad J_\varepsilon = 2 + \frac{I_4}{I_2} \ . \tag{57}$$

The damping times τ_i which also enter in the electron beam sizes, are given by:

$$\tau_i = \frac{3T_0}{J_i r_e \gamma^3 I_2} \quad i = x, z, \delta \ . \tag{58}$$

The horizontal r.m.s. emittance ε_x and the relative r.m.s. energy spread σ_δ:

$$\varepsilon_x = C_q \frac{\gamma^2}{J_x} \frac{I_5}{I_2} \quad \sigma_\delta^2 = C_q \frac{\gamma^2}{J_\delta} \frac{I_3}{I_2} \tag{59}$$

where T_0 is the revolution time of an electron, $r_e = 2.82 \times 10^{-15}$ m is the classical radius of an electron and $C_q = 3.84 \times 10^{-13}$ m.

In general, the contribution of the insertion device magnetic field to these is a small perturbation compared to those produced by the storage ring bending magnets. On a ring like the ESRF, all insertion devices contribute less than 10% to the energy loss per turn U_0; the remaining 90% is generated in the dipole magnets. On the contrary, high field superconducting wigglers installed on a low-energy ring may dramatically affect the lattice and bring modifications to the synchrotron radiation integrals. A particular sort of wiggler, called damping wiggler, is sometimes installed on a straight section of a ring in the aim of strongly modifying the synchrotron radiation integrals. To be efficient such wigglers must increase I_2 by, say, more than a factor 2 over the contributions from all bending magnets. As a result, damping wigglers must have a high field and/or be very long and/or the

bending magnet must have a low field. Damping wigglers increase the energy loss per turn and shrink the damping time, thereby reducing the sensitivity to instabilities. If they are placed in a straight section with no dispersion, they contribute to a reduction of the emittance, which is of prime interest to the users. Nevertheless, damping wigglers are rarely implemented because of a lack of space. The practical interest of damping wigglers is mainly linked with large circumference rings originally designed for high-energy physics having a low magnetic field in the bending magnets such as the LEP ring at CERN, or the PETRA ring at DESY in view of its re-conversion as a synchrotron source.

6.2 Beam deflection and focusing

Another important class of effects come from the deflection and focusing induced by the field of an insertion device. In a fixed orthogonal reference frame Ox, Oz, Os, the electron trajectory can be described by the functions $x(s)$ and $z(s)$ describing the horizontal and vertical position as a function of the longitudinal coordinate s. $x(s)$ and $z(s)$ satisfy the following equation that can be derived from the Lorentz force (3):

$$\begin{aligned} x'' &= -\frac{e}{\gamma mc}\sqrt{1+x'^2+z'^2}\left[z'B_s-(1+x'^2)B_z+x'z'B_x\right] \\ z'' &= \frac{e}{\gamma mc}\sqrt{1+x'^2+z'^2}\left[x'B_s-(1+z'^2)B_x+x'z'B_z\right] \end{aligned} \tag{60}$$

where $x'=\frac{dx}{ds}$ and $x''=\frac{d^2x}{ds^2}$ and B_x, B_z, B_s are the horizontal, vertical and longitudinal components of the magnetic field. Integrating (60) over the length L of the insertion device to the second order in the inverse of the electron energy $1/\gamma$, and making use of the fact that the magnetic field satisfies the Maxwell Equations in free space ($\vec{\nabla}\vec{B}=0$, $\vec{\nabla}\times\vec{B}=0$) gives [14]:

$$\begin{aligned} \frac{dx}{ds}(L) &= \frac{dx}{ds}(0)+\frac{e}{\gamma mc}\int_0^L B_z ds-\frac{1}{2}\left(\frac{e}{\gamma mc}\right)^2\int_0^L\frac{\partial\Phi}{\partial x}ds+o\left(\frac{1}{\gamma^2}\right) \\ \frac{dz}{ds}(L) &= \frac{dz}{ds}(0)-\frac{e}{\gamma mc}\int_0^L B_x ds-\frac{1}{2}\left(\frac{e}{\gamma mc}\right)^2\int_0^L\frac{\partial\Phi}{\partial z}ds+o\left(\frac{1}{\gamma^2}\right) \end{aligned} \tag{61}$$

where the insertion device magnetic field extends in a domain of *s* going from 0 to *L* and $o\left(\frac{1}{\gamma^2}\right)$ is a function of order $1/\gamma^3$ or higher and the function $\Phi(x,z,s)$ is given by:

$$\Phi(x,z,s)=\left(\int_0^s B_x(x,z,s')ds'\right)^2+\left(\int_0^s B_z(x,z,s')ds'\right)^2 . \tag{62}$$

Let θ_x, θ_z be the horizontal and vertical deflecting angles experienced by an electron when passing through an insertion device. It is clear from (61) that at first order in $1/\gamma$, θ_x, θ_z are expressed as:

$$\theta_x=\frac{e}{\gamma mc}\int_0^L B_z ds \quad \theta_z=-\frac{e}{\gamma mc}\int_0^L B_x ds . \tag{63}$$

In a storage ring, an electron passes through the same insertion device every turn. Each turn its trajectory is bent by the angles θ_x, θ_z. The overall result is a distortion of the closed orbit over the whole ring circumference, which in the horizontal plane can be expressed as [14]:

$$\delta x(s) = \theta_x \sqrt{\beta_x(s)\beta_x^{ID}}\,\frac{\cos(\pi\upsilon_x - \left|\phi_x(s) - \phi_x^{ID}\right|)}{2\sin(\pi\upsilon_x)} \tag{64}$$

where $\delta x(s)$, $\beta_x(s)$, $\phi_x(s)$ are the orbit displacement, horizontal beta function and betatron phase at the position *s* along the circumference. β_x^{ID}, ϕ_x^{ID} are the horizontal beta function and betatron phase at the location of the insertion device. υ_x is the horizontal betatron tune. Similarly the vertical deflecting angle θ_z is responsible for a vertical closed orbit distortion which is given by (64) replacing the horizontal betatron function and tune by the vertical ones. In a synchrotron light source, the orbit stability is of prime importance. Any deviation with time of the position of the closed orbit generates mismatching in the beamlines and therefore undesirable discontinuities in the recorded data. A common specification is to maintain the r.m.s. closed orbit distortion within 1/10th of the r.m.s. beam size. Taking the example of the ESRF, this results in a specification for the vertical (horizontal) field integral of ~ 40 (20) Gcm. This is usually sufficient for most beamline users. Nevertheless, several facilities report a few experiments that can be disturbed by an electron beam motion of the order of 1/100th of the r.m.s. beam size. It is therefore of prime importance to correct the variation of field integrals generated when the user varies the peak field $\hat{B}$.

Differentiating θ_x, θ_z with respect to *x* and *z*, one derives the focusing induced by an insertion device which involves two independent focal lengths F and F_c:

$$\begin{aligned}
\frac{1}{F} &= -\frac{\partial\theta_z}{\partial z} = \frac{\partial\theta_x}{\partial x} = \frac{e}{\gamma mc}\int_0^L \frac{\partial B_x}{\partial z}\,ds = \frac{e}{\gamma mc}\int_0^L \frac{\partial B_z}{\partial x}\,ds \\
\frac{1}{F_c} &= \frac{\partial\theta_x}{\partial z} = \frac{\partial\theta_z}{\partial x} = \frac{e}{\gamma mc}\int_0^L \frac{\partial B_z}{\partial z}\,ds = -\frac{e}{\gamma mc}\int_0^L \frac{\partial B_x}{\partial x}\,ds\ .
\end{aligned} \tag{65}$$

The focal lengths F and F_c are associated with a conventional normal and skew focusing component identical in nature to those generated by a quadrupole. Higher order derivatives of θ_x, θ_z in *x* and *z* give sextupolar, octupolar, ect. field components.

The focusing elements of the transport (quadrupole, bending magnet with gradient, etc.) maintain a so-called betatron oscillation in both the horizontal and vertical planes. In a storage ring, this oscillation is characterized by the horizontal and vertical betatron tunes ν_x and ν_z which are defined as the number of oscillations taking place over the circumference. The additional focusing induced by an insertion device generate at first order a betatron tune shifts $\delta\nu_x$ and $\delta\nu_z$ given by [14]:

$$\delta\nu_x \simeq \frac{1}{4\pi}\frac{\overline{\beta_x}}{F} \quad \delta\nu_z \simeq \frac{1}{4\pi}\frac{\overline{\beta_z}}{F} \quad \delta\nu_c \simeq \frac{1}{4\pi}\frac{\sqrt{\overline{\beta_x}\,\overline{\beta_z}}}{F_c} \tag{66}$$

where $\overline{\beta_x}$ and $\overline{\beta_z}$ are the unperturbed horizontal and vertical beta functions averaged over the length of the insertion device. The skew focal length F_c is responsible for a coupling of the horizontal and vertical betatron oscillation characterized by the coupling tune $\delta\nu_c$. A detailed analysis of this tune shift can be traced to the occurrence of a small oscillation of the beta functions (beta beat) over the whole circumference which relative amplitude $\frac{\Delta\beta_x}{\beta_x}$, $\frac{\Delta\beta_z}{\beta_z}$ is expressed as:

$$\frac{\Delta\beta_x}{\beta_x} = \frac{2\pi\delta\upsilon_x}{\sin(2\pi\upsilon_x)} \quad \frac{\Delta\beta_z}{\beta_z} = \frac{2\pi\delta\upsilon_z}{\sin(2\pi\upsilon_z)} \quad . \tag{67}$$

Such tune shifts are undesirable. It may bring the tune closer to some resonance where the beam becomes excited. The variation of the beta function also generates an undesirable change of the beam sizes and divergences on each beamline. Higher derivatives of the field integrals vs. x and z may result in increased chromaticity or additional non-linearities in the betatron motion. In the worst case such additional non-linearities may reduce the dynamic aperture and reduce the lifetime of the stored beam. The magnet lattice of modern low emittance third generation sources has a precise compensation for the non-linearities induced by the sextupole magnets. A small modification of the beta functions produced by a single insertion device may break this compensation and again reduce the dynamic aperture and the lifetime.

For the reasons developed above, it is important to eliminate such field integrals and their derivatives vs. x and z. Indeed, almost all insertion devices can be designed with zero field integrals. It is a matter of properly designing the field terminations and of correcting the field errors induced by magnetic imperfections in the permanent magnet blocks or those due to positioning errors of the individual blocks in the full assembly. This is done by carefully measuring and tuning the field either by displacing blocks or by adding iron sheets at the surface of the assembly. The process is called multipole shimming. Ultimately, when performed with sufficient care, the multipole shimming removes most the variations of the deflections θ_x, θ_z vs. *x* and *z*, leaving a residual constant offset which can be corrected using small coils located at each extremity of the device. Unfortunately, this is not the end of the story. So far we have discussed the contributions linear to $1/\gamma$ in (61). Closed orbit distortions, focusing and beta beat are also induced at second order in $1/\gamma$. Such effects are numerically computed through the function $\Phi(x,z,s)$ by means of equations (61) and (62). The deflecting angles at second order in $1/\gamma$ are deduced from (61):

$$\begin{aligned} \theta_x &= -\frac{1}{2}\left(\frac{e}{\gamma mc}\right)^2 \int_0^L \frac{\partial\Phi}{\partial x} ds \\ \theta_z &= -\frac{1}{2}\left(\frac{e}{\gamma mc}\right)^2 \int_0^L \frac{\partial\Phi}{\partial z} ds \quad . \end{aligned} \tag{68}$$

The derivatives of the deflective angle determine the focusing effects characterized by the three focal lengths F_x, F_z and F_c:

$$\frac{1}{F_x} = \frac{\partial \theta_x}{\partial x} = -\frac{1}{2}\left(\frac{e}{\gamma mc}\right)^2 \int_0^L \frac{\partial^2 \Phi}{\partial x^2} ds$$
$$\frac{1}{F_z} = \frac{\partial \theta_z}{\partial z} = -\frac{1}{2}\left(\frac{e}{\gamma mc}\right)^2 \int_0^L \frac{\partial^2 \Phi}{\partial z^2} ds \qquad (69)$$
$$\frac{1}{F_c} = \frac{\partial \theta_x}{\partial z} = \frac{\partial \theta_z}{\partial x} = -\frac{1}{2}\left(\frac{e}{\gamma mc}\right)^2 \int_0^L \frac{\partial^2 \Phi}{\partial x \partial z} ds \ .$$

The numerical computation of θ_x, θ_z and its derivatives with respect to x and z largely depend on the nature of the function Φ, which is itself a function of the transverse components of the magnetic field expressed by (62). At this stage, we will limit the discussion to the conventional planar insertion which presents a symmetry axis (the normal beam axis) such that:

$$B_x = \frac{\partial B_x}{\partial x} = \frac{\partial B_z}{\partial z} = \frac{\partial B_x}{\partial z} = \frac{\partial B_z}{\partial x} = 0 \ . \qquad (70)$$

Replacing (70) into (61), one derives:

$$\theta_x = 0$$
$$\theta_z = 0$$
$$\frac{1}{F_x} + \frac{1}{F_z} = \left(\frac{e}{\gamma mc}\right)^2 \int_0^L B_z^2 ds \qquad (71)$$
$$\frac{1}{F_z} = \left(\frac{e}{\gamma mc}\right)^2 \left(\int_0^L B_z^2 ds - \int_0^L \int_0^s \frac{\partial^2 B_z}{\partial x^2} ds' \int_0^s B_z ds' ds \right)$$
$$\frac{1}{F_c} = 0 \ .$$

In the particular case where $\frac{\partial^2 B_z}{\partial x^2} = 0$, one then obtains

$$\frac{1}{F_z} = \left(\frac{e}{\gamma mc}\right)^2 \int_0^L B_z^2 ds$$
$$\frac{1}{F_x} = \frac{1}{F_c} = 0 \ . \qquad (72)$$

In other words, a conventional planar undulator essentially produces a vertical focusing proportional to the integral of the square of the field and inversely proportional to the electron energy. In real undulators and wigglers, the vertical field is at its maximum on axis of the device and decays slowly in the medium plane away from the axis. As a result, there is a small horizontal defocusing effect on axis expressed by (71). The deflection and focusing properties described above have been derived in a somewhat abstract way by means of solving the differential equation (60) . One can understand the focusing produced by an undulator as follows. At first order in $1/\gamma$, the vertical field create a sinusoidal horizontal velocity and trajectory. Applying again the Lorentz force equation and making the vector product of the $1/\gamma$ horizontal velocity with the longitudinal component of the field generates a vertical force and therefore an angular deflection linear in $1/\gamma^2$. In the median plane, the longitudinal component of the field is zero, and there is no vertical deflection in $1/\gamma^2$. The

longitudinal component of the field appears only away from the median plane linearly in *z*. As a result the vertical deflection is linear to *z* which makes a vertical focusing. Contrary to the focusing proportional to $1/\gamma$ that can be locally corrected, such types of focusing cannot be removed without removing the main magnetic field. Note also that it cannot be simply compensated locally by means of a quadrupole-type lens placed at the extremity because such a lens would only remove the vertical focusing by adding some horizontal defocusing. Most synchrotron light sources operate at a sufficiently high electron energy meaning that such focusing is usually small and simply requires a global adjustment of the tunes.

7 Insertion device technology

7.1 2D analytical field computation

There are only two sources of magnetic field available to magnet engineers, namely currents and permanent magnet materials. Embedding them into an iron yoke allows the generation of a higher magnetic field and/or a better control of the field pattern. The simplest type of undulator that one can imagine is an array of current carrying elements with current flowing alternatively in opposite directions. This is schematized in Fig. 12:

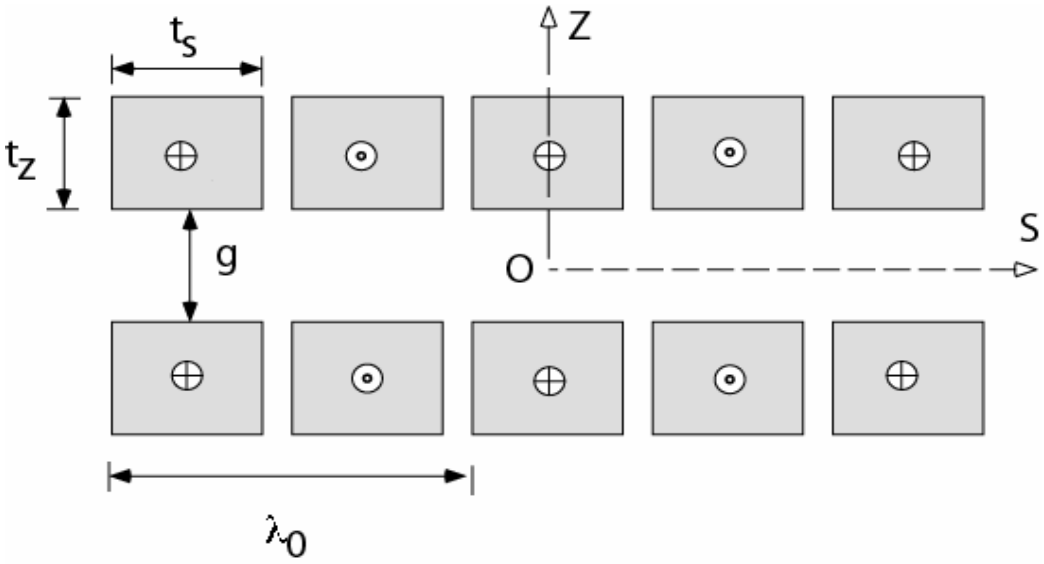

Fig. 12: Array of current carrying elements generating an undulator type magnetic field. The beam passes in the median plane along Os

Assuming infinitely long conductors, the vertical field experienced not, by an electron travelling in the median plane along Os at equal distance between the upper and lower conductor arrays is a periodic function of the period λ_0 expressed by [16]:

$$B_z(s) = \sum_{n=1,3,5} \frac{4\mu_0 I}{\lambda_0} \exp(-n\pi \frac{g+t_z}{\lambda_0}) \frac{\sin(n\pi t_s/\lambda_0)}{n\pi t_s/\lambda_0} \frac{\sinh(n\pi t_z/\lambda_0)}{n\pi t_z/\lambda_0} \sin(2\pi n \frac{s}{\lambda_0}) \,, \qquad (73)$$

where I is the total current in each conductor, g is the magnetic gap between the upper and lower arrays of conductors and t_z and t_s are the conductor dimensions as defined in Fig. 12. In most cases of interest, the harmonic $n = 1$ dominates and the field is nearly sinusoidal. Similarly, a common and straightforward method of generating a periodic field using permanent magnets is to assemble them as shown in Fig. 13.

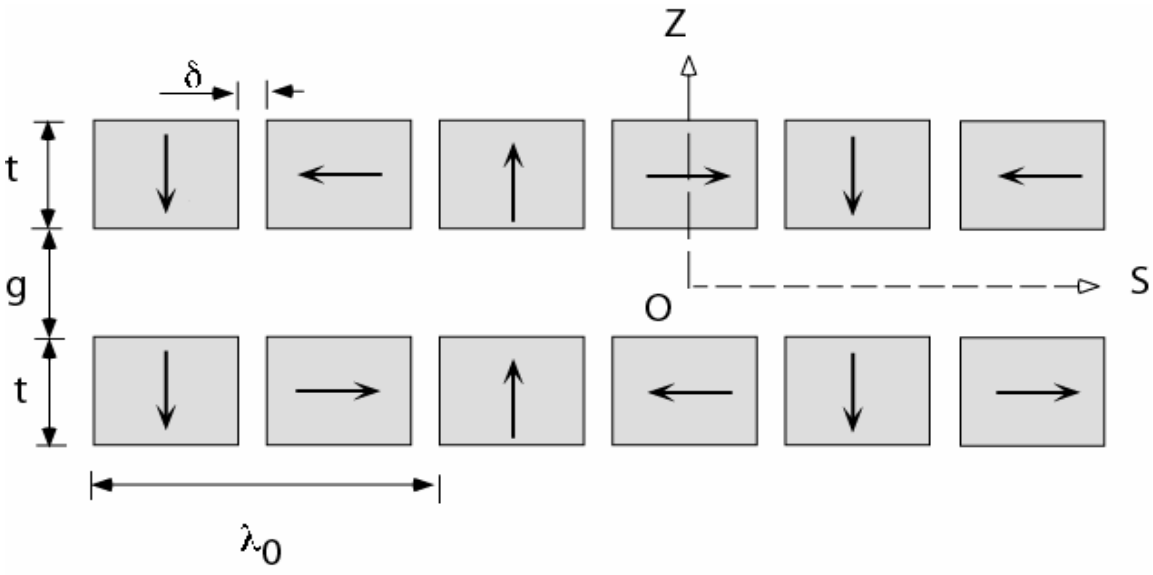

Fig. 13: Array of permanent magnets generating an undulator type magnetic field. The electron beam passes in the median plane along Os. The arrow defines the direction of the magnetization.

Assuming infinitely long permanent magnets in the direction perpendicular to the figure, one derives the vertical field seen by the beam in the median plane [17]:

$$B_z(s) = 2\mu_0 M \sum_{n=1,5,9,..} \exp(-n\pi \frac{g}{\lambda_0}) \frac{\sin(n\pi(1/4 - \delta/\lambda_0))}{n\pi/4} \times (1 - \exp(-2\pi n \frac{t}{\lambda_0})) \sin(2\pi n \frac{s}{\lambda_0}) \quad (74)$$

where M is the magnetization of the permanent magnet material, g is the gap between the upper and lower magnet array, λ_0 is the period and t, δ are defined in Fig. 13. Again for practical values for the gap and period, the field is dominated by the fundamental *n* = 1 component. In the typical case where $\delta = 0$ and $t = \lambda_0/2$, the field of the first harmonic reduces to

$$B_z(s) = 1.72\mu_0 M \exp(-\pi \frac{g}{\lambda_0}) \sin(2\pi \frac{s}{\lambda_0}) \quad . \quad (75)$$

Increasing the thickness t of the magnet beyond $\lambda_0/2$ to infinity only gives 4% more field on the fundamental. A typical permanent magnet material needed to build an undulator requires a high remanent field B_r as well as a high coercivite field. These properties are achieved by the NdFeB alloys which present a typical B_r of 1.2–1.3 T. The Sm_2Co_{17} alloy is also used sometimes. It has a lower B_r around 1.05 T, but presents a higher Curie temperature resulting in a remanent field less sensitive to temperature variations. Sm_2Co_{17} is also less sensitive to radiation damage. Both materials, when magnetized, have a small relative permeability around their operating point resulting in $M \simeq B_r$.

Let $\hat{B}_I$ be the peak field created by a current undulator (as in Fig. 12) and $\hat{B}_M$ the peak field created by a permanent magnet undulator (as in Fig. 13) of same period and gap and similar dimension $t_s = t_z = t = \lambda_0/2$. Their ratio is deduced from (74) and (75):

$$\frac{\hat{B}_I}{\hat{B}_M} = 0.45\frac{I}{\lambda_0 M} \approx 0.11\mu_0 \frac{\lambda_0 J}{B_r} \tag{76}$$

where μ_0 is the vacuum permeability, J is the current density in the conductor and B_r is the remanent field of the permanent magnet material. For a 30 mm period undulator and a NdFeB material with a remanent field B_r of 1.2 T, one requires a current density of more than 280 A/mm^2 to reach the same field. Such a current density can only be achieved using superconducting technology. In common room-temperature electromagnet undulators, one reinforces the field by using an iron yoke, but staying with current densities below 5 A/mm^2, which is, in most cases, insufficient to compete with permanent magnets. One is now in a position to understand why **the large majority of undulators and wigglers are built with permanent magnets** rather than current and yoke. Indeed the magnetic structure presented in Fig. 13 has been selected for a very large number of undulators. To obtain more fields one can also use hybrid technology in which narrow pieces of iron are inserted between the magnets as shown in Fig. 14:

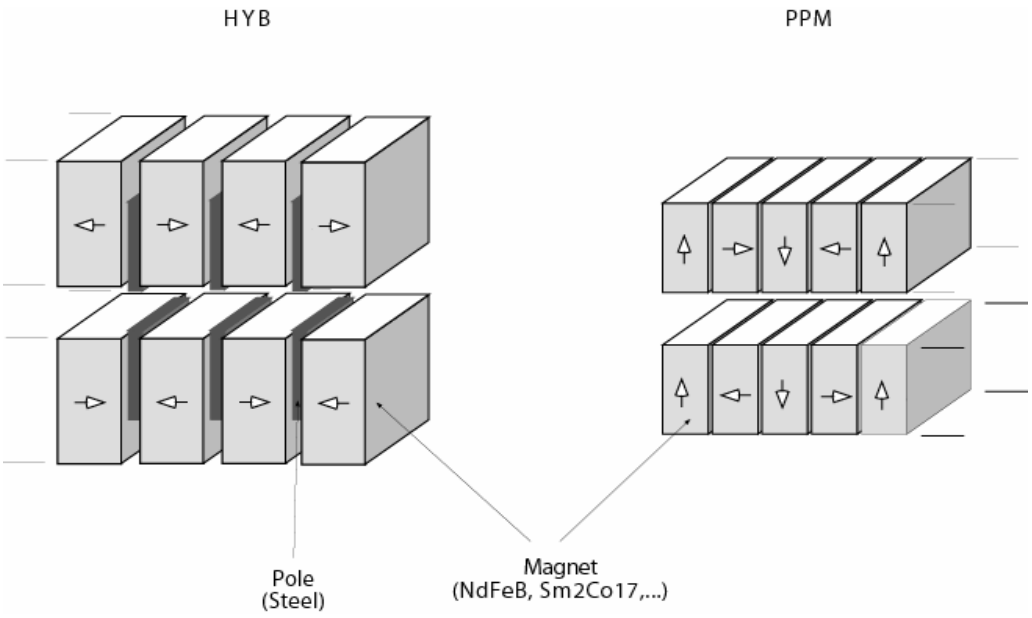

Fig. 14: The two most popular magnet structures used to build undulators and wigglers. On the right is the Pure Permanent Magnet (PPM) structure. On the left is the hybrid structure where pieces of iron are inserted between the blocks of permanent magnets. The arrows indicate the direction of magnetisation. The electron beam passes in the middle of the gap between the upper and lower magnet arrays.

7.2 3D field computation

The magnetic field produced by a hybrid structure is slightly larger than that produced by a pure permanent magnet structure. Figure 15 presents a comparison of the peak field and the first harmonic of the Fourier decomposition for a pure permanent magnet device, a hybrid structure with poles made from an ARMCO steel (inexpensive steel) and a hybrid device with poles made of Vanadium Permendur (highest performance). It appears from Fig. 15 that the first harmonic deviates only slightly

from the peak field. The pure permanent magnet array saturates its peak field with a lower volume of magnets as compared to the hybrid. The advantage in peak field of the hybrid over the pure permanent magnet array really occurs if a large volume of magnets is used.

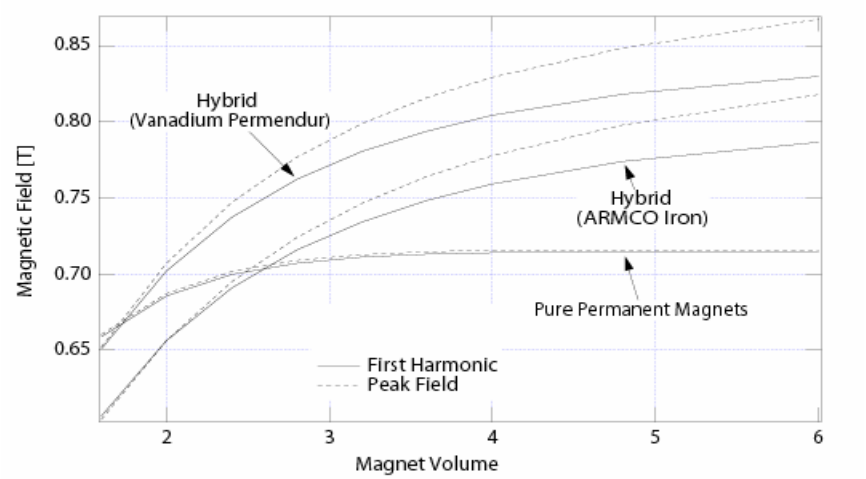

Fig. 15: Peak field (dash curves) and first harmonic (plain curves) of the field as a function of the total permanent magnet volume in units of $N\lambda_0^3$ for a pure permanent magnet array and hybrid type structure with poles made either of ARMCO or Vanadium Permendur. In all three cases, the horizontal width of the block has been set to $2\lambda_0$ and the ratio of the gap/period is 0.314. For each magnet volume all free parameters are optimised to maximize the peak field.

Finally, Fig. 16 presents a comparison of peak field and first harmonic as a function of the gap/period ratio. For a large gap the advantage of the hybrid technology is marginal while with a small gap, the most difference is seen with an increasing contribution from the harmonics higher than 1.

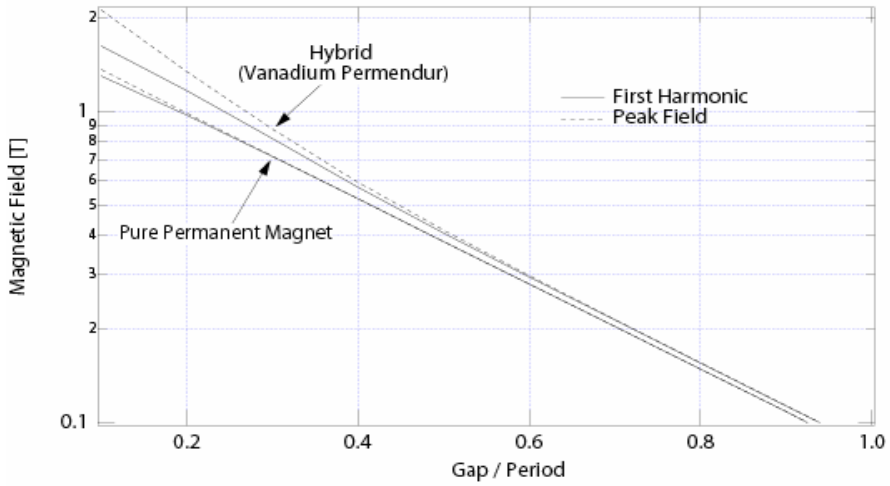

Fig. 16: Peak field and first harmonic as a function of the ratio of the magnetic gap to period for a pure permanent magnet structure and a hybrid structure with pole made of Vanadium Permendur. In both cases the horizontal width of the magnets is equal to twice the period, and the volume of magnet per period is equal to $2\lambda_0^3$. For gap/period, and within the constraint of a limited volume and fixed horizontal dimension, the dimensions of the magnets and blocks have been optimized to maximize the peak field.

Figures 15 and 16 have been computed using the 3D magnetostatic code RADIA [18] which makes use of the so-called volume integral method. Similar computations can be made from the various commercially available packages making use of finite elements such as TOSCA [19], FLUX3D [20], MAXWELL [21], ANSYS [22]. As discussed above, most undulators and wigglers are made of permanent magnets. In order to vary the peak field of such a device, the only method is to change the magnetic gap. In the particular case of the pure permanent magnet arrays, (74) allows a precise estimation of the peak field at any gap and period. In most situations where the fundamental dominates, (75) is much simpler to use. There is no such universal and simple formula as (75) for a hybrid structure that relates the peak field or the fundamental as a function of period and gap. The following empirical relationship is often used to estimate the achievable peak field $\hat{B}$ based on a series of 2D calculations with optimized poles and magnet dimensions :

$$\hat{B} = a \exp\left(-b\frac{g}{\lambda_0} + c(\frac{g}{\lambda_0})^2 \right) \tag{77}$$

where a = 3.33, b = 5.47 , c = 1.8 for a $SmCo_5$ material with B_r = 0.9 T [23] and a = 3.44, b = 5.08 , c = 1.54 for NdFeB material with B_r = 1.1 T [24] . Such formula has been established for $0.07 \le \frac{g}{\lambda_0} \le 0.7$ The formula expressed in (77) is handy to obtain a rough estimate of the achievable peak field. It is not precise since a, b and c depend on the magnet coercivity, remanent field and overall volume of magnetic material. In addition it does not give any information on the harmonic content. Indeed, contrary to the pure permanent magnet undulator which contains harmonic 1.5.9, in the field, the hybrid undulator contains all odd harmonics : 1,3,5,… Finally this formula does not apply if one optimizes an undulator at some gap and wants to estimate the field that such undulator would produce at a larger gap. Such formulas were more useful ten years ago when 3D magnetostatic computation were imprecise due to the lack of software and CPU power. Nowadays, most designers derive the peak field as well as the field harmonic content numerically using one of the software packages mentioned above.

7.3 Variable-gap support structures

The large field generated by an undulator results in a large magnetic force between the upper and lower arrays. For a sinusoidal field undulator or wiggler, the force F can be derived by integrating the Maxwell Tensor over the undulator median plane. It yields:

$$F \simeq \frac{1}{4\mu_0}\hat{B}^2 LW \tag{78}$$

where L is the length of the undulator and W is the horizontal width of the magnet array. For a 2 m long device with a 100 mm horizontal width and a 1 Tesla peak field, this force amounts to 40 000 N! As a result, a strong support structure is needed to guide the gap motion. In addition, it is clear from (75) that the field is highly sensitive to the gap and one must minimize the gap variation along the length of the structure if one needs a constant peak field along the structure. This is particularly important for undulators for which the spectrum of the radiation is made up of a set of narrow peaks the energy of which varies with K and therefore with the field and therefore with the gap. A large gap variation along the structure would broaden the peaks. In other words the supporting structure holding the magnet arrays must be stiff enough to minimize the deflection under the heavy magnetic load. Figure 17 presents such a support structure in use for the many insertion devices at the ESRF. It is a so-called C type structure in which the rigid frame holding both girders occupies only a single side of the magnet array. Such a C type structure allows the installation or removal of an insertion device

without having to break the vacuum of the ring. The alternative is an H type structure where the supporting takes place on both sides and generates a lower deflection. H type structures are usually only preferred for very high field devices generating large magnetic forces. The installation of H type structures requires breaking the vacuum in the straight section upon installation. The gap change on such a structure is carried out by powering one or two high torque motors equipped with proper demultiplication.

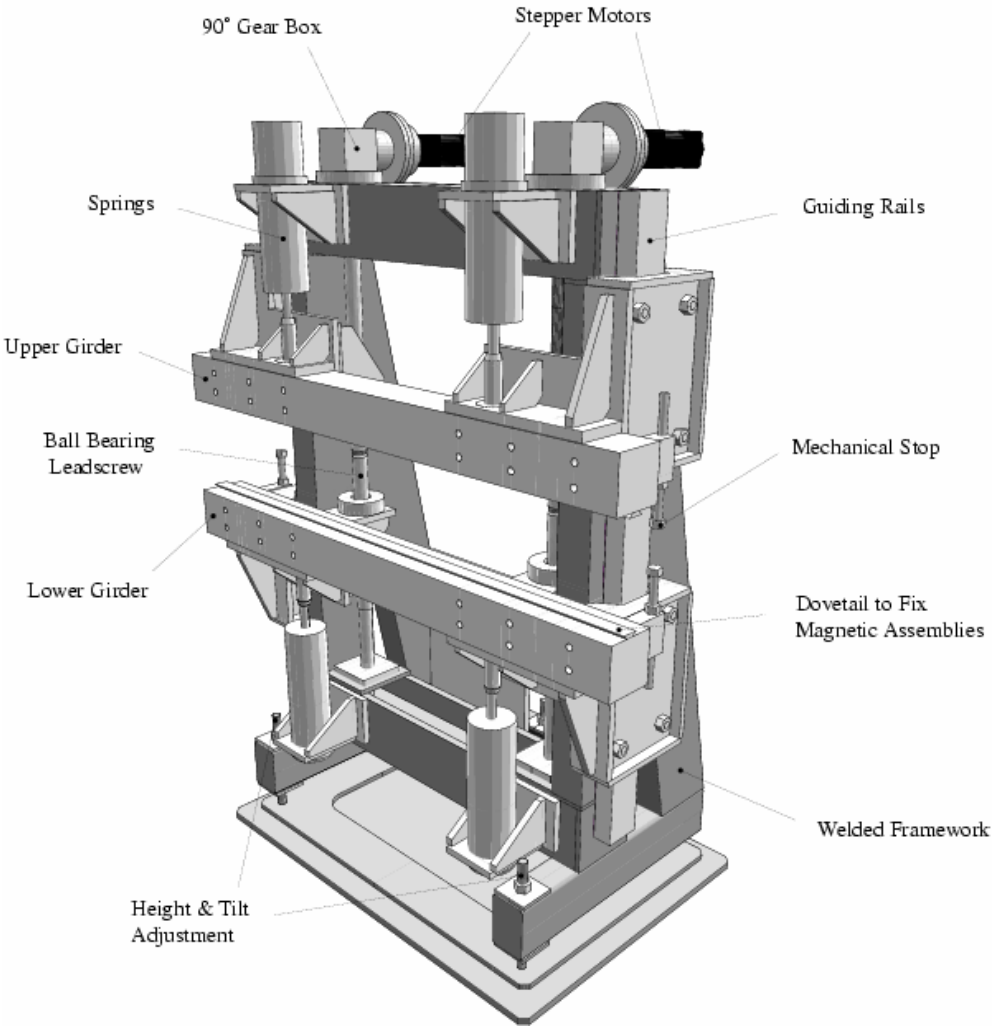

Fig. 17: ESRF support structure holding the magnet arrays and capable of tuning the magnetic gap over a range of 300 mm with a resolution of 1 µm while withstanding magnetic forces as high as 100 000 N with limited deformation of the girder. The permanent magnet arrays are fixed to the rigid girders by means of the dovetail profile.

A recent evolution of undulator technology has been to reach very small magnetic gaps. This pressure is drawn from the requirement to push the fundamental photon energy of an undulator spectrum to higher energy. A typical undulator system is 5 m long and is operated with a magnetic gap close to 10 mm. The magnet blocks are located in the air outside of a narrow aperture and flat and thin wall vacuum chamber where the electron beam circulates in ultra high vacuum. This chamber is usually made of aluminium with wall thickness less than 1 mm leaving less than an 8mm vertical aperture to the electron beam. The narrow aperture and the long length of the undulator results in a poor vacuum, which is undesirable since it generates bremsstrahlung in the associated beamline. Pumping is either made by a ribbon of Non Evaporable Getter (NEG) material placed along the chamber close to the beam in a so-called anti-chamber (APS type chamber), or by evaporating a thin

film of NEG material on the internal wall of the chamber (ESRF type chambers). In both cases the NEG needs to be activated to a higher temperature in order to ensure the correct pumping speed.

7.4 In-vacuum undulators

If a smaller magnetic gap is required, then one must use the so-called in-vacuum undulator technology developed at NSLS [25], Bessy [26], Photon factory [27], SPring-8 [28] and ESRF [29]. Several years ago this technology was considered as somewhat adventurous. Nowadays, though still tricky, it has become mature and is now commercially available following the large-scale implementation on the Spring-8 storage ring. The magnet blocks are placed inside the vacuum chamber. To be compatible with the ultra high vacuum, the magnet blocks need to be coated with a ultra high vacuum compatible material such as Nickel or TiN. The magnet surface is covered by a thin sheet (~0.1 mm) of a sandwich of copper and nickel. The copper conducts the return current from the beam and avoids excessive heatload deposition in the blocks while the nickel adds a constant attraction force of the sheet towards the magnet array and maintains the sheet in contact with the magnets. Figure 18 presents a 3D view of such an in-vacuum undulator as built at the ESRF.

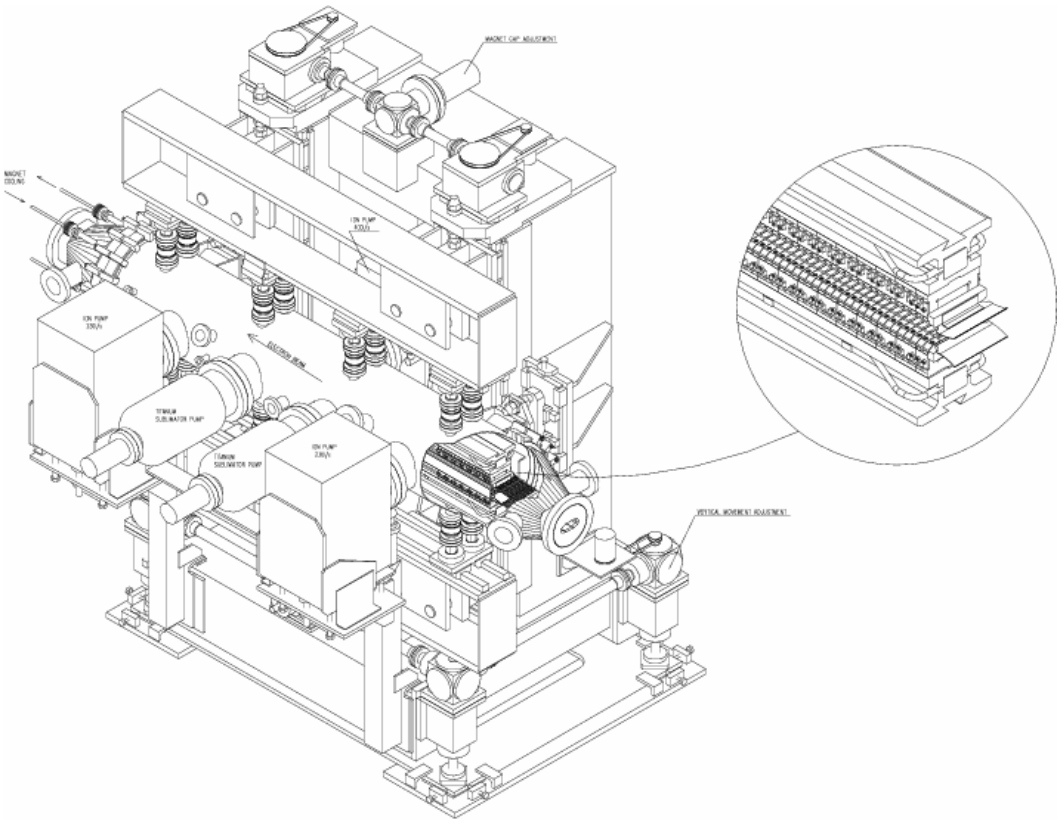

Fig. 18: 3D view of an ESRF in-vacuum undulator. Illustration from Ref. [9].

7.5 Phase errors

The magnetic field from undulators and wigglers must satisfy three types of specifications. The first types of specifications are the user specifications, which are the field geometry, period and number of periods. These must be selected in order to reach the desired photon energy range with the desired flux and brilliance within the heatload constraints that the beamline is capable of handling. The second class of specifications concerns the integrated multipole components (both normal and skew) that must be sufficiently small in order to prevent closed orbit distortion, tune shifts and possible reduction of dynamic aperture (see section above). The third class of specifications concerns only undulators, the peak field and period of which must be stable to a fraction of a per cent along the length of the

device if one wants to keep narrow high harmonic peaks in the spectrum. To address this question more quantitatively, let us define the phase advance Φ_p of the p[th] pole of the magnetic field at the wavelength λ:

$$\Phi_p = \frac{\pi}{\lambda\gamma^2}\left[\int_{Pole\ p} 1+\gamma^2(\vartheta_x^2(s)+\vartheta_z^2(s))ds\right] \tag{79}$$

where $\vartheta_x(s)$ and $\vartheta_x(s)$ are the horizontal electron velocities defined as

$$\vartheta_x(s) = \frac{e}{\gamma mc}\int_{-\infty}^{s} B_z(s)ds \quad \vartheta_z(s) = -\frac{e}{\gamma mc}\int_{-\infty}^{s} B_x(s)ds \ . \tag{80}$$

The whole range of longitudinal coordinates is partitioned into a number of consecutive poles. The partition points are defined as the points where the $\vartheta_x^2(s)+\vartheta_z^2(s)$ reach a local minimum as a function of *s*. The naming of the pole can be traced to the case of an ideal hybrid undulator for which the partition points fall exactly in the middle of an iron pole. Equations (1) and (2) can be expressed as :

$$\frac{d\Phi}{d\Omega d\omega/\omega} \propto \left|\sum_p e^{i\Phi_p}\right|^2 \tag{81}$$

If the wavelength λ is equal to the fundamental undulator wavelength and if the field is an ideal sinewave then all Φ_p are equal to π and $\left|\sum_p e^{i\Phi_p}\right|^2 = 4N^2$. Field errors generate some fluctuations of Φ_p from one period to the next. Assuming that the phase errors are independent and uncorrelated from one pole to the next with an r.m.s. fluctuation σ_Φ (also called phase error), then the angular spectral flux given by (81) is reduced to:

$$\frac{d\Phi}{d\Omega d\omega/\omega} \propto \left|\sum_p e^{i\Phi_p}\right|^2 = 4N^2\exp(-\sigma_\Phi^2) \ . \tag{82}$$

Both the phases Φ_p and phase errors σ_Φ scale like $1/\lambda$, therefore the reduction of the angular spectral flux due to the phase errors induced by magnetic imperfections are strongly dependent on the harmonic number. The higher the harmonic the higher the reduction. Table 2 presents a computation of $e^{-\sigma_\Phi^2}$ as a function of harmonic number for two different cases of r.m.s. phase errors of 1° and 6° degrees computed on the fundamental wavelength λ_1. A phase error of 6° corresponds to a typical undulator assembled from permanent magnets without any particular precautions for correcting such phase errors, while a 1° phase error corresponds to a specially shimmed undulator (see below). Clearly, undulators used on the fundamental are rather insensitive to phase errors. On the other hand, operating an undulator on a high harmonic with high flux and brilliance requires special care in removing phase errors.

Table 2: Reduction of the angular spectral flux as a function of harmonics and r.m.s. phase error.

Harmonic #	$\sigma_\Phi = 6°$	$\sigma_\Phi = 1°$
1	0.99	1
5	0.76	0.99
9	0.41	0.98
13	0.16	0.95

Contrary to the dipole or quadrupole magnets, permanent magnet undulators are not iron-dominated magnets. This is not only true for pure permanent magnet undulators but also for hybrid undulators in which the major part of the field is not created by the magnetized iron but by the permanent magnet material itself. As a consequence, the precise field profile is very sensitive to the variation of magnetization from one magnet block to the next as well as to the precise position of each block in the array. In addition, while all magnetic blocks are specified identically, the magnetization is usually not 100% uniform in the block: depending on the manufacturing process, there can be significant non-uniformities. While the manufacturer of an iron-dominated magnet must essentially be careful with regard to the precision of machining of the yoke (the non-uniform magnetic permeability is usually low), the manufacturer of a permanent magnet undulator or wiggler must limit the deviations from one magnet block to another. The blocks must usually be measured one by one in an effort to cancel their variations of magnetization by suitable pairing during the assembly process. If done with the utmost rigour this work is enormous (typical undulators such as the 100 period undulator include 800 magnet blocks), although it is rarely carried through to the required precision. In addition small random position errors during assembly add new types of errors. As a result an assembled undulator is rarely within the desired specifications in terms of both multipole errors and phase errors. Some further shimming must be carried out. Shimming can be achieved either by displacing some of the blocks or by adding small thin pieces of iron (50 microns typical) on the surface of the blocks as shown in Fig. 19. In general it is preferable to tune the field errors by displacing magnet blocks or a pole whenever possible rather than adding iron shims that always shortcut some of the flux generated by the blocks.

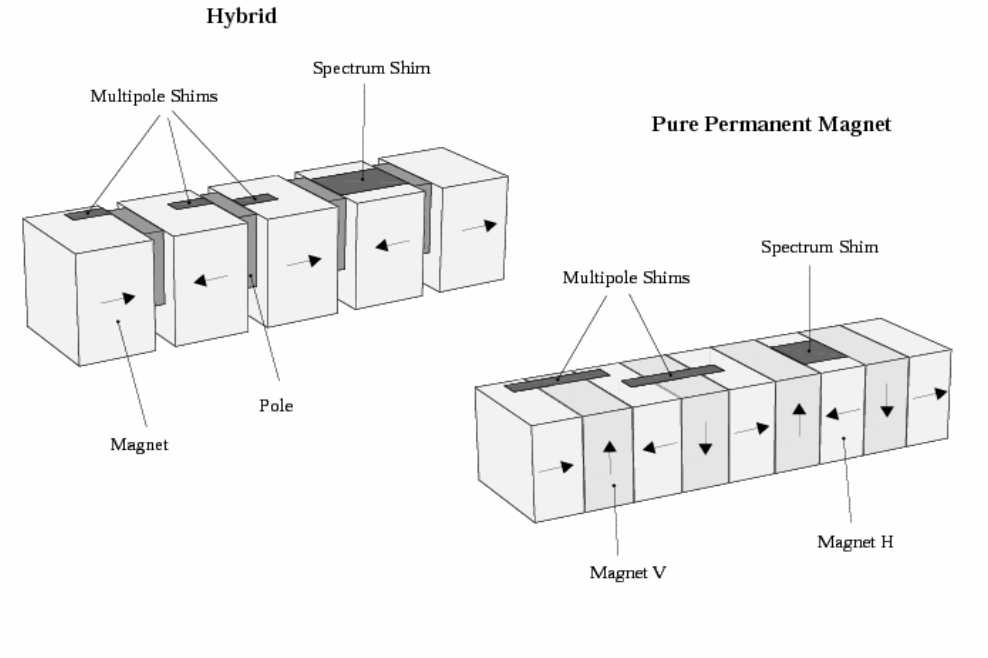

Fig. 19: Multipole and spectrum (phase) shims on a pure permanent magnet array (PPM) or a hybrid array (HYB)

8 Insertion devices for circular polarization

So far we have discussed the properties and engineering of conventional insertion devices with a planar, nearly sinusoidal magnetic field. These undulators and wigglers essentially produce linearly polarized radiation with an electric field perpendicular to the plane of the undulator magnetic field. For some scientific applications, it is important to produce circularly polarized radiation. There exists a number of different types of insertion design optimised to generate such radiation. We shall not review them extensively. The reader interested in more detail should consult Refs. [3,30]. We shall only discuss in more detail the most successful of such undulators known as Apple II [31]-[33]. Apple II undulators are now present in almost all synchrotron light sources. The magnet array of an Apple II undulator is shown in Fig. 20.

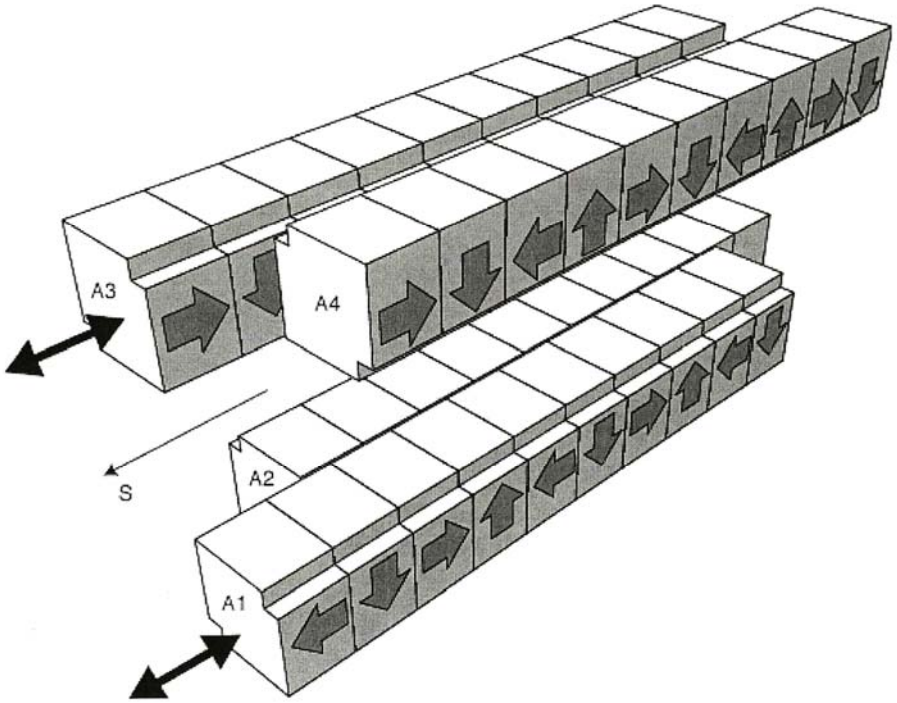

Fig. 20: Magnet array of an Apple II undulator

The magnet array can be described as a pure permanent magnet array where the upper and lower arrays have been cut into two independent arrays, the longitudinal position of which can be changed with respect to each other. Let us number the magnet arrays as A1, A2, A3 and A4 as shown in Fig. 20. Let us first consider the situation in which the A2 and A4 magnet arrays stay in position while the A1 and A3 arrays are moved longitudinally by the same quantity δ. One can then show that the transverse components of the magnetic field seen by the beam is, in general, ellipsoidal:

$$B_z(s) = 4B_{z0}\cos(\frac{\varphi}{2})\cos(2\pi\frac{s}{\lambda_0}+\frac{\varphi}{2})$$
$$B_x(s) = -4B_{x0}\sin(\frac{\varphi}{2})\sin(2\pi\frac{s}{\lambda_0}+\frac{\varphi}{2}) \quad (83)$$

where $\varphi = 2\pi\frac{\delta}{\lambda_0}$ and B_{z0} and B_{x0} vary with the magnetic gap between the upper and lower magnet arrays. Depending on the displacement δ, the field can be linear vertical, ellipsoidal, circular or linear horizontal. The three most important limiting cases are:

$$\delta = 0 \Rightarrow [B_z(s), B_x(s)] = [4B_{z0}\cos(2\pi\frac{s}{\lambda_0}), 0] \quad \text{vertical field}$$

$$\delta = \frac{\lambda_0}{2} \Rightarrow [B_z(s), B_x(s)] = [0, -4B_{x0}\sin(2\pi\frac{s}{\lambda_0})] \quad \text{horizontal field} \tag{84}$$

$$\delta = \frac{\lambda_0}{\pi}\tan^{-1}(\frac{B_{x0}}{B_{z0}}) \Rightarrow \quad [B_z(s), B_x(s)] = B\left[\cos(2\pi\frac{s}{\lambda_0}+\frac{\varphi}{2}), -\sin(2\pi\frac{s}{\lambda_0}+\frac{\varphi}{2})\right] \quad \text{helical field}$$

If, on the other hand, one displaces the A1 and A3 magnet arrays in opposite directions but with the same quantity δ, then the magnetic field seen by the beam is:

$$[B_z(s), B_x(s)] = \left[4B_{z0}\cos^2(\frac{\varphi}{2}), -4B_{x0}\sin^2(\frac{\varphi}{2})\right]\cos(2\pi\frac{s}{\lambda_0}) \tag{85}$$

This defines a linearly polarized magnetic field with orientation continuously rotating from vertical to horizontal as $\varphi = 2\pi\frac{\delta}{\lambda_0}$ varies from 0 to π.

As just discussed, the magnetic field generated by an Apple II is extremely flexible. One can show that for a given gap and period the field in whichever polarization state is close to the highest that one can design. These properties of flexible polarization and field efficiency are the reason for the success of the Apple II undulator. Contrary to a conventional planar device where only the gap is a free parameter, an Apple II undulator is built with three degrees of freedom, namely the magnetic gap and the longitudinal positions of both the A1 and A3 magnet arrays. From the engineering point of view the field tuning of an Apple II undulator is more tricky since the integrated multipoles must be insensitive to any of the three degrees of freedom. Apple II undulators also present a variation of the second order focusing (focusing inversely proportional to the inverse of the square of the electron energy, see Section 6) as a function of the longitudinal position of the A1 and A3 magnet arrays. This requires special attention, especially on a low-energy storage ring.

9 Undulators for free electron lasers

Finally it is difficult to conclude this lecture on insertion devices without briefly mentioning the special kind of undulators needed for the new free electron laser projects. The most ambitious Free Electron Lasers (FELs) are based on the Self Amplified Spontaneous Emission (SASE). In a SASE FEL, the synchrotron radiation produced in the entrance of the undulator is re-amplified as the electrons travels further inside the undulator. The process saturates at a very large field and the SASE radiation generated can be more monochromatic and brilliant than synchrotron radiation also called (by analogy with classical lasers) spontaneous emission.

In order to have enough gain and to saturate the laser power over a limited length of undulator, ultra short electron bunches with low energy spread and emittance are needed. Such electron beam characteristics are not available from a storage ring; but from a linear accelerator injected with recently developed ultra low emittance electron guns. Nevertheless the undulators need to be long. The shorter the targeted wavelength, the higher the electron energy and the longer the undulator. For an ultimate 0.1 nm wavelength FEL (LCLS project at SLAC and XFEL project at DESY), one estimates that the electron energy will need to be in the 15-20 GeV range and the undulator will be 100 to 200 m long. Such long undulators need to be split into segments of few metres length as shown in Fig. 21. The undulator can either be of the planar type or helical. The amplification per unit length of undulator (also called the growth length) is higher in a helical undulator than in a planar undulator.

This makes the total length of a helical undulator shorter. Nevertheless many projects still rely on the planar type permanent magnet based structure which is the best known and mastered.

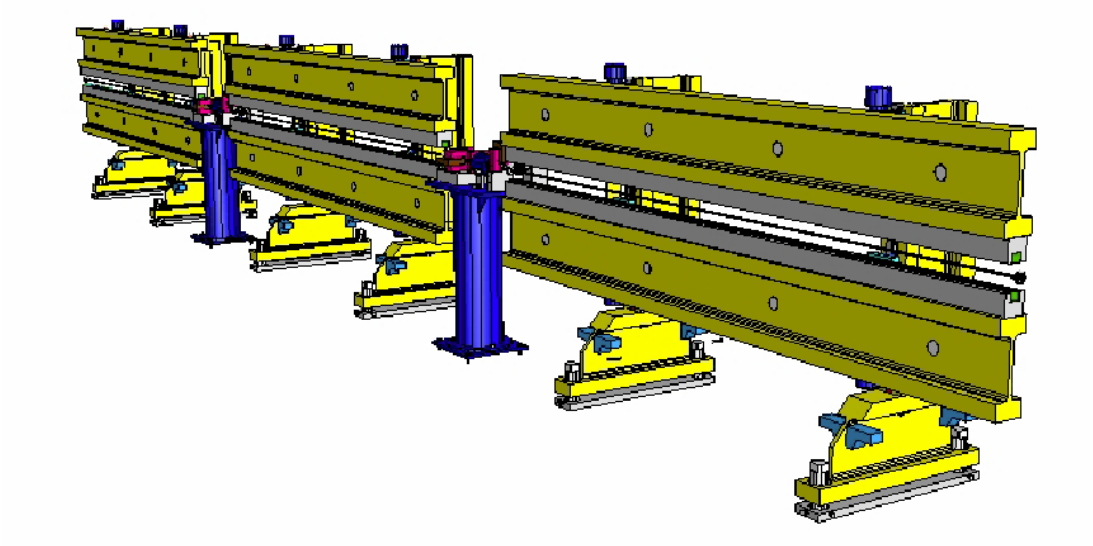

Fig. 21: 3D conceptual design of the XFEL undulator. A large number of variable gap vertical field undulators of about 3 m length are separated by diagnostic stations.

The undulator segments are spaced a few tens of centimetres from each other. The sections between undulators include:

- quadrupole focusing for maintaining a small electron beam size all along the device,
- steerers to align the electron beam in each undulator section,
- three-pole phasing section to delay the electron bunch and ensure a proper phasing of the undulator sections,
- electron-beam-position monitors.

Contrary to storage ring type undulators, the magnetic specification of the SASE undulator segments are quite relaxed both in terms of integrated multipoles and phase errors. This is due to the fact that electrons only pass once in the undulator and that only the fundamental of the spectrum is really amplified. One of the challenging issues is the required alignment of the electron beam axis to the radiation beam to a precision of a few micrometers over the full 100-200 m length. Such an alignment requires sophisticated electron and photon beam based alignment techniques. Another challenging issue is the organization of the series production and measurement and tuning of such undulator segments by industry. The reader interested in more information concerning the design and manufacture of very long SASE undulators should consult Refs. [34]-[39].

References

[1] Winick, H., R.H. Helm, *Nucl. Instrum. Meth.* **152** (1978) 9.

[2] *Undulators, Wigglers and Their Applications*, Editor H. Onuki, P. Elleaume, Taylor & Francis, London 2003.

[3] Walker, R.P., *Insertion Device: Undulators and Wigglers*, CERN Accelerator School: Synchrotron Radiation and Free Electron Lasers, Grenoble, France, 22 - 27 Apr 1996, p 129.

[4] Kim, K. J., *Characteristics of Synchrotron Radiation*, AIP Conference Proceedings 184, p. 567 (American Institute of Physics, New York, 1989). vol. 1,

[5] Jackson, J.D., *Classical Electrodynamics*, (John Wiley & Sons Inc., New York, 1962) Chapter 14.

[6] Elleaume P., Ref. [2], Chapter 2.

[7] Walker, R.P. Ref. [2], Chapter 4.

[8] Elleaume P., Ref. [2], Chapter 3.

[9] B2E, available from http://www.esrf.fr/machine/groups/insertion_devices/Codes/software.html

[10] SPECTRA, available from http://www.spring8.or.jp/e/facility/bl/insertion/Softs/index.html

[11] SRW, available from http://www.esrf.fr/machine/groups/insertion_devices/Codes/software.html

[12] Walker, R.P. and B. Diviacco, *Rev. Sci. Instrum.* **63** (1992) 392.

[13] XOP, available from http://www.esrf.fr/computing/scientific/xop/

[14] Farvacque L., Ref. [2], Chapter 1.

[15] Elleaume P., Proc EPAC 92 Conference, Berlin.

[16] Elleaume P., Ref. [2], Chapter 5.

[17] Halbach, K., *Nucl. Instrum. Meth*. **187** (1981) 109-117.

[18] P. Elleaume, O. Chubar, J. Chavanne, "Computing 3D Magnetics Fields from Insertion Devices", Proceedings of the PAC97 Conference, May 1997, pp. 3509-3511. O. Chubar, P. Elleaume, J. Chavanne, "A 3D Magnetostatics Computer Code for Insertion devices", *Synchr. Rad*. **5** (1998) 481-484

[19] TOSCA, Vector Fields Limited, Oxford, England, see "http://www.vectorfields.co.uk/"

[20] FLUX3D, Cedrat S.A., see http://www.cedrat-grenoble.fr/

[21] MAXWEL, Ansoft Corporation, see "http://www.ansoft.com/"

[22] ANSYS, Engineering Analysis System, Swanson Analysis System Inc. see http://www.ansys.com/

[23] Halbach, K, *J. de Physique C1* **44** (1984) 211.

[24] 6 GeV Synchrotron X-ray source, Conceptual Design report, Supplement A, LS-52 , March 1986, Argonne National Laboratory.

[25] H. Hsieh, S. Krinsky, A. Luccio, C. Pellegrini, A. Van Steenbergen, *Nucl. Instrum. Meth.* **A208** (1983) 79-90, P.M. Stefan *et al*., *J. Synchr. Rad*. **5** (1998) 417-419, see also P.M. Stefan *et al. Nucl. Instr. and Methods* **A412** (1998) 161.

[26] W. Gudat, J. Pfluegher, J. Chatzipetros, W. Peatman, *Nucl. Instrum. Meth.* **A246** (1986) p. 50-53.

[27] S. Yamamoto, T. Shioya, M. Hara, H. Kitamura, X. Zhang, T. Mochizuki, H. Sugiyama, M. Ando, *Rev. Sci. Instrum*. **63** (1992) 400.

[28] T. Hara, T. Tanaka, T. Tanabe, X.M. Marechal, S. Okada, H. Kitamura, *J. Synchr. Rad.* **5** (1998) 403-405.

[29] J. Chavanne, P. Elleaume, P. Van Vaerenbergh, Proc. of the 1999 Particle Accelerator Conference, p. 2662.

[30] Onuki, H., Ref. [2] , Chapter 6.

[31] Sasaki, S., K. Miyata and T. Takada, *Jpn. J. Appl. Phys*. **31** (1992) L1794.

[32] Sasaki, S., K. Kakuno, T. Takada, T. Shimada, K. Yanagida and Y. Miyahara, *Nucl. Instrum. Meth*. **A331** (1993) 763.

[33] Sasaki, S., T. Shimada, K. Yanagida, H. Kobayashi and Y. Miyahara, *Nucl. Instrum. Meth.* **A347** (1994) 87.

[34] S. Caspi, R. Schlueter, R. Tatchyn, Proceedings of the PAC95 Conference, Dallas, TX, pp. 1441-1443.

[35] R. Schlueter, *Nucl. Instr. and Meth.* **A 358** (1995) 44.

[36] Pflueger, J., Proc. 1999 Particle Accelerator Conference.

[37] Elleaume, P., Chavanne, J., Faatz, B., *Nucl. Instum. Meth.*, **A455** (2000) 503-523.

[38] I.B. Vasserman, S. Sasaki, R.J. Dejus, E.R. Moog, E. Trakhtenberg, O. Makarov, N. Vinokurov, *Proceedings of the 24th International Free Electron Laser Conference and 9th Annual FEL User Workshop,* Argonne, IL, USA, 9-13 Sep 2002.

[39] TESLA -XFEL, Technical Design report,
http://tesla.desy.de/new_pages/tdr_update/supplement.html